

# Automating Crystal-Structure Phase Mapping: Combining Deep Learning with Constraint Reasoning

Di Chen<sup>1</sup>, Yiwei Bai<sup>1</sup>, Sebastian Ament<sup>1</sup>, Wenting Zhao<sup>1</sup>, Dan Guevarra<sup>2</sup>, Lan Zhou<sup>2</sup>, Bart Selman<sup>1</sup>, R. Bruce van Dover<sup>3</sup>, John M. Gregoire<sup>2,4,†</sup> & Carla P. Gomes<sup>1,†</sup>

<sup>1</sup> Cornell University, Department of Computer Science

<sup>2</sup> California Institute of Technology, Joint Center for Artificial Photosynthesis

<sup>3</sup> Cornell University, Department of Materials Science and Engineering

<sup>4</sup> California Institute of Technology, Division of Engineering and Applied Science

† Corresponding authors: gomes@cs.cornell.edu and gregoire@caltech.edu.

Crystal-structure phase mapping is a core, long-standing challenge in materials science that requires identifying crystal structures, or mixtures thereof, in synthesized materials. Materials science experts excel at solving simple systems but cannot solve complex systems, creating a major bottleneck in high-throughput materials discovery. Herein we show how to automate crystal-structure phase mapping. We formulate phase mapping as an unsupervised pattern demixing problem and describe how to solve it using Deep Reasoning Networks (DRNets). DRNets combine deep learning with constraint reasoning for incorporating scientific prior knowledge and consequently require only a modest amount of (unlabeled) data. DRNets compensate for the limited data by exploiting and magnifying the rich prior-knowledge about the thermodynamic rules governing the mixtures of crystals with constraint reasoning seamlessly integrated into neural network optimization. DRNets are designed with an interpretable latent space for encoding prior-knowledge domain constraints and seamlessly integrate constraint reasoning into neural network optimization. DRNets surpass previous approaches on crystal-structure phase mapping, unraveling the Bi-Cu-V oxide phase diagram, and aiding the discovery of solar-fuels materials.

Artificial Intelligence (AI)<sup>1</sup> aims to develop intelligent systems, inspired in part by human intelligence. AI systems are now performing at human and even superhuman levels on a range of tasks such as image identification<sup>2</sup>, face,<sup>3</sup> and speech recognition<sup>4</sup>. AI also has the potential to accelerate scientific discovery dramatically.<sup>5–10</sup> Recent AI achievements have been driven mainly by advances in supervised deep learning<sup>11</sup>, which requires large labeled datasets to supervise model training. However, in general, scientists do not have large amounts of labeled data for scientific discovery. They often solve complex tasks using only a few data samples by amplifying intuitive pattern recognition with detailed reasoning about prior knowledge to make sense of the data. Such a hybrid strategy has been difficult to automate. Herein we consider crystal-structure phase mapping, a long standing challenge in materials science that is emblematic of the class of scientific problems whose automation constitutes a substantial advancement with respect to the grand challenge of high-throughput unsupervised scientific data interpretation.

Crystal-structure phase mapping involves separating noisy mixtures of X-ray diffraction (XRD) patterns into the source XRD signals of the corresponding crystal structures, a task for

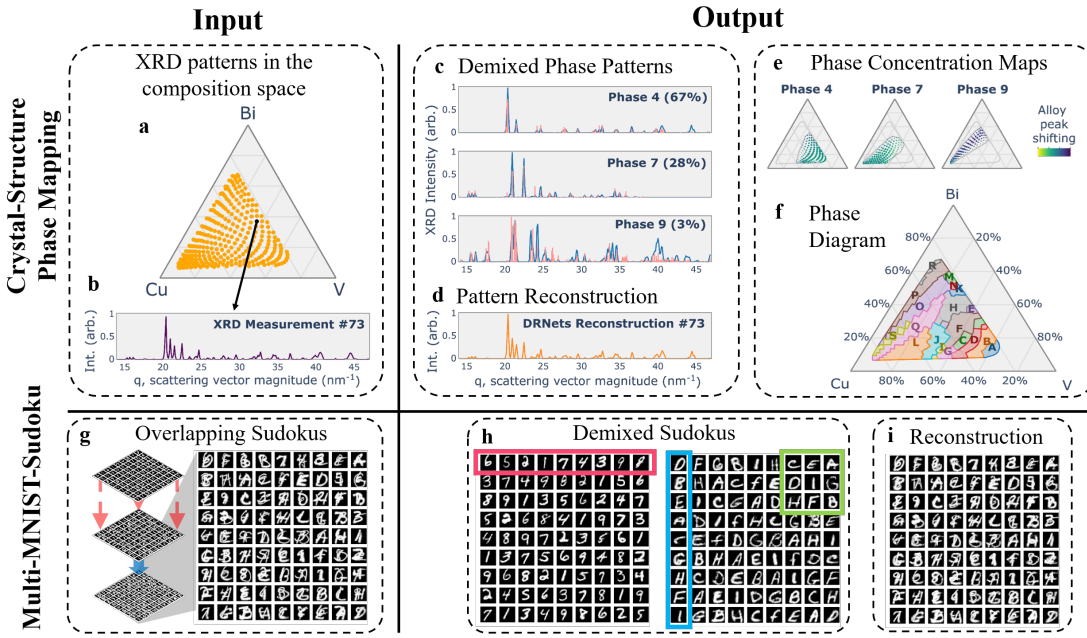


**Figure 1: Crystal-Structure Phase Mapping and Multi-MNIST-Sudoku** Phase mapping is a demixing task wherein a phase diagram is inferred from a set of XRD patterns in a materials composition space (**a**), requiring identification of pure-phase prototypes and their composition-dependent modification. The input (**a-b**) and output (**c-f**) are illustrated for pattern #73 where the DRNets-modified prototypes are shown as sticks in (**c**) for each demixed pattern. For each phase, DRNets output includes the composition map of activation and alloying-based modification from the prototype, shown in (**e**) for 3 phases. The composition regions corresponding to each unique combination of phases is the most salient aspect of the underlying phase diagram (**f**). In a 9x9 Sudoku, the cells in each row (red rectangle), column (blue rectangle), and any of the nine non-overlapping 3x3 boxes (green square) have all-different digits. In Multi-MNIST-Sudoku (**g**), the goal is to demix the digits into the two original Sudokus (**h**), closely reconstructing the original input images (**i**).

which labeled training data are typically not available. Furthermore, a valid phase diagram of the crystal structures of a given chemical system must satisfy thermodynamics rules (Fig. 1a-f). Herein we provide a detailed description of how to formulate phase mapping as an unsupervised pattern demixing problem and how to solve it using Deep Reasoning Networks (DRNets)<sup>12</sup>. DRNets are a general framework for combining deep learning with constraint reasoning for incorporating scientific prior knowledge. DRNets are designed with an interpretable latent space for encoding the prior-knowledge domain constraints, enabling seamless integration of constraint reasoning into neural network optimization. Constraint reasoning is a particular type of AI reasoning in which axioms and rules are expressed as constraints and the inference procedure is a search method. The axioms and rules pertaining to a given task comprise the prior knowledge needed to identify valid solutions. In this manuscript, we show how DRNets require only a modest amount of (unlabeled) data and compensate for the limited data by exploiting and magnifying the rich scientific prior knowledge about the thermodynamic rules that govern the mixtures of crystals. We further provide

insights concerning the interpretability and scalability of DRNets, as well as the role of data and the different DRNets’ modules, through a series of ablation studies. DRNets make this crystal-structure phase mapping advancement by combining learning with constraint reasoning, emulating the analysis of expert scientists and enabling interpretation of complex systems in high-dimensional composition spaces.

Given the scientific complexity of Crystal-Structure Phase Mapping, we provide an initial intuitive explanation of DRNets framework based on Multi-MNIST-Sudoku,<sup>12</sup> a variant of the Sudoku game that involves demixing two completed overlapping hand-written Sudokus (Fig. 1g-i). To demonstrate the scalability of DRNets, we also consider 9x9 Sudoku instances combining *both digits and letters*, beyond the 4x4 Multi-MNIST-Sudoku instances involving only digits, used in the original Multi-MNIST-Sudoku variant<sup>12</sup>. We note that, in addition to its intuitive allure, Sudoku represents a logical reasoning task and is a computationally hard combinatorial problem<sup>13</sup>. Thus, Multi-MNIST-Sudoku, with hand-written digits and letters, encapsulates a hybrid reasoning-learning task and provides a tangible demonstration of the value of integrating learning and reasoning for noisy data. The availability of ground truth data also facilitates algorithm comparisons and ablation studies.

Deep Reasoning Networks (DRNets) provide a general framework that integrates pattern recognition with reasoning about prior knowledge. Both Crystal-Structure Phase Mapping and Multi-MNIST-Sudoku involve identification and demixing of the component signals in mixed-signal input data, specifically crystal phases or handwritten digits and letters. Moreover, for scientific tasks such as crystal structure phase mapping, researchers generally only have access to at most a few hundred (unlabeled) data samples, which greatly challenges classical data-hungry supervised deep learning models. Therefore, to tackle such unsupervised demixing tasks, supervision by constraint reasoning is required and supported by extensive prior knowledge from sources ranging from fundamental physical principles to the intuitive experience of scientists. More specifically, both demixing tasks involve two types of prior knowledge: prototypes of the component signals and rules that govern their mixtures. Both demixing tasks require constraint reasoning to interpret noisy and uncertain data, while satisfying a set of rules: thermodynamic rules, and Sudoku rules, respectively. When considering complex data instances with multiple composition degrees of freedom and many constituent phases, crystal structure phase mapping is substantially more complex than Multi-MNIST-Sudoku and can even surpass the analytical capabilities of human experts.

Complex constraints, such as the thermodynamic rules of phase mapping, are ubiquitous in the physical sciences. Constraint satisfaction and optimization is an impactful approach for domains ranging from satisfiability to sphere packing and protein folding,<sup>14–16</sup> and is an approach we have explored for phase mapping.<sup>17</sup> The lack of labeled data combined with the realities of experimental data, such as noise and deviations of measured patterns from their idealized prototypes, require simultaneous learning of the de-mixed signals and reasoning about their mixtures, making constraint satisfaction necessary but insufficient for phase mapping solvers. DRNets encode complex constraints via a meaningful and interpretable latent representation coupled with a fixed generative

decoder that captures the prior knowledge about the domain patterns in an end-to-end deep net framework. Furthermore, the constraint reasoning of DRNets enhances the learning of the shared parameters that govern pattern mixing across multiple (unlabeled) input instances, which in turn facilitates demixing of each pattern in the source dataset. The goal of the present work is to demonstrate the impact of this seamless integration of reasoning and learning for unsupervised pattern demixing tasks, Multi-MNIST-Sudoku as an illustrative example and ultimately crystal structure phase mapping, which are solved by the same general DRNets framework customized with task-specific component models. DRNets for phase mapping tackle a core long standing problem in materials science, outperforming prior methods, which is demonstrated on a benchmark system and by solving the previously unsolved Bi-Cu-V oxide phase diagram. The results contribute to the broader goal of establishing DRNets as a modular end-to-end framework for tasks that require integrating pattern recognition capabilities with reasoning about prior knowledge, which are pervasive in scientific areas as diverse as biology, materials science, and medicine.

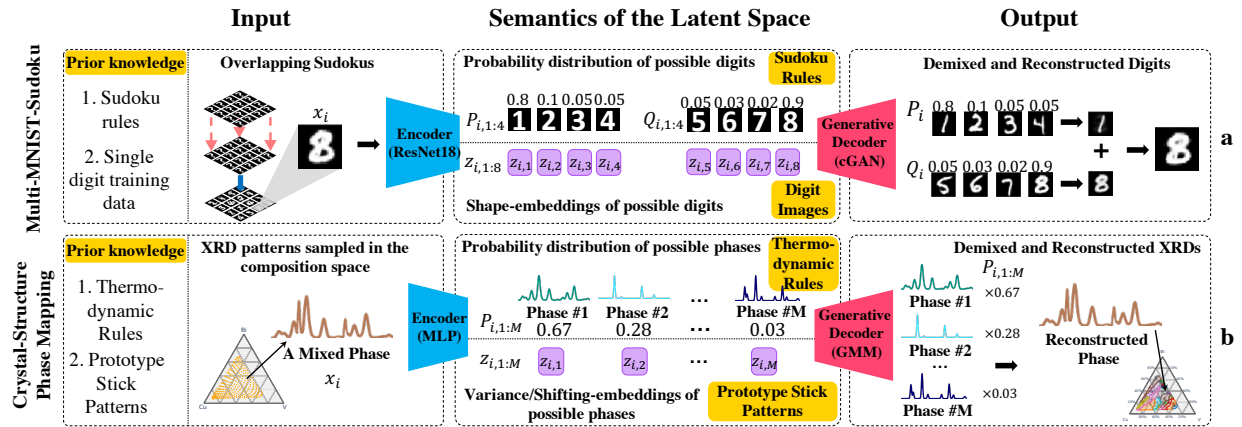


Figure 2: **DRNets framework and the semantics of the latent space for different tasks.** In the DRNets framework, an *interpretable* structured latent space is key to incorporating prior knowledge, through the interplay of the encoder, the generative decoder (cGAN trained on single digits or a Gaussian Mixture Model (GMM) based on prototype stick patterns), and the reasoning constraints (Sudoku rules or thermodynamic rules). **a.** In **Multi-MNIST-Sudoku**, DRNets encode the input overlapping digits  $x_i$  into  $P_{i,1:4}$ ,  $Q_{i,1:4}$  and  $z_{i,1:8}$ , which denote the probability distribution and the shape embedding of possible digits (1-8). The generative-decoder (cGAN) uses  $z_{i,1:8}$  to generate the demixed hand-written digits and reconstruct the original input with the expected overlapping image using  $P_{i,1:4}$  and  $Q_{i,1:4}$ . **b.** In **crystal-structure phase mapping**, DRNets encode the input XRD pattern  $x_i$  into  $P_{i,1:M}$  and  $z_{i,1:M}$ , which denote the probability distribution and the variance/shifting-embedding of  $M$  possible phases. The generative-decoder (GMM) uses  $z_{i,1:M}$  to generate the decomposed phases and reconstruct the original XRD using the phase probability distribution  $P_{i,1:M}$ .

## DRNets framework

At a high level, the goal of unsupervised pattern demixing of crystal structures or digits and letters is to infer the base patterns underlying the mixtures observed in unlabeled data.<sup>18</sup> The demixing task

is therefore to invert the pattern mixing processes from the data, i.e., the generative processes for each pattern and the way the patterns are combined. However, often unlabeled data do not provide a strong enough pattern signal, motivating reasoning about prior knowledge. DRNets enhance standard unsupervised pattern discovery approaches with prior knowledge about the constraints that govern the patterns, via constraint reasoning, and prior knowledge about the patterns' *shape*, via a fixed generative decoder (see Fig. 2). More specifically, DRNets combine deep learning with constraint reasoning in an *end-to-end encoder-generative-decoder framework*, and formulate unsupervised pattern discovery as a *data-driven constrained optimization problem* that (i) minimizes a reconstruction loss of the input data, such that (ii) the inferred patterns adhere to a given generative model and (iii) satisfy domain constraints. See mathematical details about DRNets' problem formulation flow in Extended Data Fig. 1 and [Methods](#).

While standard machine learning approaches can easily handle (i), enforcing (ii) and (iii) is challenging and emblematic of the limitations of traditional deep learning. The standard approach for incorporating domain knowledge into a deep net architecture is to add terms to the loss function such as various types of sparsity constraints. However, we need to encode more complex constraints, such as combinatorial constraints to express valid Sudoku solutions or thermodynamic rules. For example, a digit cannot appear more than once in a row or an X-ray diffraction pattern cannot be explained by more than 3 prototype phases, or 2 prototype phases if there is alloying. *The challenge of our demixing tasks is that the domain rules capturing prior knowledge involve variables that we do not have direct access to in our problem formulation. In fact, discovering those variables and their values is part of the interpretation task that we are trying to solve.* The challenge is further complicated by the fact that we are operating in an unsupervised setting (no labeled training data). In supervised learning, different strategies have been exploited to incorporate prior knowledge, ranging from placing constraints on the output variables of the deep net to hybrid approaches interleaving symbolic and neural processing.<sup>19</sup> However, in standard unsupervised deep learning approaches, e.g., neural networks autoencoders, the latent space is generally uninterpretable and therefore does not provide a means to express the domain constraints or enforce that the latent patterns conform to the generative model. Furthermore, domain rules are often captured by combinatorial constraints that are not differentiable, and therefore cannot be easily embedded in a deep learning framework. The strategy in DRNets to overcome these challenges is to (1) specify *an intended semantics* for the latent space, which means that the latent space is constructed using variables that have a specific interpretation that can be used in the formulation of the domain rules. For example, in the Sudoku domain, we will introduce a latent variable for each possible digit that gives the probability of that digit being present in the cell associated with the input image. We can now use these variables in constraints on the allowed combinations of digits (see Fig. 2). As we will show, these latent variables take on the desired semantics using a small set of unlabeled examples combined with the encoded domain constraints; (2) express the domain rules that control the encoding of the latent space in a form amenable to continuous optimization using *entropy-based continuous relaxations*; (3) employ *an optimization formulation whose objective balances the dual needs of minimizing a reconstruction loss of the input data and a reasoning loss that captures the domain constraints* (local constraints involving a single data point or global constraints involving many data points);

(4) use a data-driven approach to jointly solve multiple related (unlabeled) data instances; and (5) solve the data-driven constrained optimization problem using *constraint-aware stochastic gradient descent*, a variant of stochastic gradient descent developed for DRNets that batches together data points involved in the same constraints and is aware of the constraints, automatically adjusting the weights of the constraints as a function of their satisfiability.

In DRNets, learning is data driven and reasoning is knowledge driven. Two intertwined processes combine learning and reasoning to discover the values for the encoder's parameters that provide the best interpretation for the interpretable latent space, given the data and prior knowledge: input pattern reconstruction (digits and crystal phases) in conjunction with reasoning about the domain rules (Sudoku and thermodynamic rules). The input pattern reconstruction is performed through the reconstruction loss, with guidance from prototypical domain patterns (single digits and crystal phases) provided via a fixed generative decoder. The reasoning is performed with "self-supervision" from the domain rules prior knowledge, encoded as constraints using the interpretable latent space variables and added as entropy-based continuous functions to the loss via Lagrangean relaxation. The reconstruction and reasoning loss constrain the encoding of the latent space to adhere to the domain patterns and rules. We refer to DRNets' formulation as *data-driven constrained optimization* to highlight that even though we design an interpretable latent-space, its semantics are ultimately determined by the quality and quantity of the (unlabeled) data as well as the prior knowledge available, which are critical for conditioning the optimization process to discover the underlying patterns and pattern mixing process across instances. Since often the pattern mixing function is not invertible, the optimization process in DRNets is further conditioned by learning the shared mixing process parameters across instances (e.g. multiple Sudoku instances or related X-ray diffraction patterns). In contrast, standard direct optimization typically considers one instance at a time. Interestingly, as our ablation studies show, while multiple (unlabeled) data are required by DRNets to uncover the pattern mixing process, the amount of (unlabeled) data required is considerably more modest than in standard supervised deep learning settings (see Fig. 6 and Extended Data Fig. 2). Further details about DRNets' problem formulation flow, constraint relaxations, and DRNets' algorithms are given in Extended Data Fig. 1, [Methods](#), and [Supplementary Methods](#).

### Sudoku: demixing handwritten digits and letters

Multi-MNIST-Sudoku consists of demixing digits from two completed overlapping hand-written Sudokus while satisfying Sudoku rules (Fig. 1a-c). The prior knowledge comprises the information that a set of images forms two overlapping handwritten Sudokus; each image corresponds to a Sudoku cell with two overlapping handwritten digits/letters; and the Sudoku rules (Fig. 1f). Humans tackle Multi-MNIST-Sudoku by interleaving vision clues with reasoning about Sudoku rules, which is emulated by DRNets as illustrated in Fig. 1d. DRNets combine deep learning with constraint reasoning and optimization to reason about Sudoku rules. In Multi-MNIST-Sudoku DRNets, a deep neural network encodes a structured latent representation of the input (digit images), which

captures the probabilities and shapes of the possible digits under Sudoku constraints enforced by the reasoning module (Fig.2a). The reasoning module comprises the reasoning constraints as well as batch and constraint weight controllers. A fixed conditional generative adversarial network (cGAN) pre-trained on single digits, incorporating prior single digit prototype knowledge, decodes (generates) the individual digit images from their structured latent representation along with their probabilities to reconstruct the mixed input image. The overall objective function of DRNets combines responses from the generative decoder and the reasoning constraints, and is optimized using constraint-aware stochastic gradient descent. We apply entropy-based probabilistic continuous relaxations to encode discrete constraints, such as Sudoku rules, which can be seamlessly incorporated into the objective function. *A key distinguishing feature of DRNets is an interpretable latent space with semantics emerging by the coupling of the encoder, the generative decoder, and reasoning module*, in contrast to standard deep learning methods in which the latent space lacks semantics. Further details about DRNets' components, latent space semantics, problem formulation, and algorithms are given in Fig. 2, Extended Data Fig. 3, and Methods.

To evaluate DRNets, we generated 32x32 images of overlapping digits/letters from the test set of MNIST<sup>20</sup> and EMNIST<sup>21</sup>, such that every  $n^2$  ( $n$  is 4 or 9) images form two n-by-n, overlapping Sudokus (see Supplementary Methods). For the 9x9 case, to distinguish the two overlapping Sudokus, we used letters A-I from EMNIST for the second Sudoku. For ease of presentation, we refer to these letters as "digits" in the following content. DRNets are unsupervised and therefore do not train on labeled mixed digit images; DRNets only have access to single hand-written digits from the MNIST/EMNIST training dataset, which are used to pre-train the generative decoder (cGAN). DRNets significantly outperform state-of-the-art supervised MNIST demixing models CapsuleNet<sup>22</sup> and ResNet<sup>23</sup>, which in contrast to DRNets are supervised by training on labeled mixed images produced by overlapping digits from the MNIST/EMNIST training dataset (Extended Data Fig. 4).

The intuitive nature of the Sudoku task provides an opportunity to gain insights regarding DRNets' structure and performance via ablation studies. For example, if we replace the fixed cGAN with a (weaker) standard learnable decoder, without prior knowledge about single digits, the optimization process can no longer find the right semantics for the latent space. Moreover, removing the reasoning module also deteriorates the digit accuracy, in addition to the Sudoku accuracy (Extended Data Fig. 4 and Supplementary Note). The final ablation study shows the importance of the data-driven learning of the shared parameters of the demixing task across multiple 9x9 Multi-MNIST-Sudoku instances. Nevertheless, DRNets can reach 99% accuracy with only 100 (unlabeled) 9x9 Multi-MNIST-Sudoku instances (Extended data Fig. 2), a considerable smaller amount of data compared to standard deep learning approaches. More generally, DRNets accomplish superior performance through *self-supervision by reasoning* about Sudoku rules, resulting in a better performance for digit accuracy and considerably better for Sudoku accuracy than the supervised systems. The broader implication is that the reasoning component enables DRNets to compensate for the lack of training data, which considerably broadens the purview of AI to problems that have a rich prior knowledge but may lack sufficient training data for traditional deep learning.

## Crystal-structure phase mapping: demixing X-Ray diffraction patterns

Scientific discovery comprises a range of problems where *self-supervision by reasoning* is strongly desired due to the lack of large example datasets, and strongly motivated by extensive prior knowledge, from fundamental principles to the intuitive experience of scientists. In materials science, phase mapping is the problem of inferring the individual phases, i.e., crystal structures, from a collection of X-ray diffraction (XRD) patterns (Fig. 1a-f), a major bottleneck in research due to the substantial expert analysis required for generating meaningful solutions<sup>24-28</sup>. As a demixing problem, phase mapping parallels the high level structure of Multi-MNIST-Sudoku where instead of overlapping handwritten digits, an XRD pattern contains a mixture of signals from so-called “pure” phases, and the solution includes demixed signals from each XRD pattern with rules based on a collection of input XRD patterns, as illustrated in Fig. 3. The prototypes in phase mapping are *stick patterns* that provide the locations and intensities of peaks in XRD patterns for each known phase (See Fig. 3 and Fig. 5), and this set of peaks comprises the entirety of the XRD signal for a single crystal structure, i.e., a pure-phase pattern. Computationally, phase mapping is an NP-hard problem<sup>17</sup> whose sheer number of possible combinations of prototypes in each XRD pattern grows exponentially with data size, ( $\sim 300$  XRD patterns and  $\sim 200$  prototypes), rendering traditional methods computationally infeasible. Supervised methods<sup>9;29-32</sup> for phase identification in an XRD pattern and unsupervised methods for phase mapping<sup>27;28;33</sup> have been developed and perform well on some datasets, especially when input patterns are akin to simple mixtures of prototypes with mutually distinguishable features. Ternary composition spaces, i.e., mixtures of 3 elements from the periodic table, have great scientific value for discovery of materials with desired properties that is concomitant with complex phase behavior in which different compositions (proportions of the elements) form many unique mixtures of the prototype phases. The complexity is compounded by phenomena such as alloying, wherein each composition’s XRD pattern may contain unique variants of the prototypes. The most typical alloying-based variation of a prototype includes altered peak intensities and systematically-shifted peak positions. Peak intensities can also vary from the prototypes due to various ways in which the materials and experiment conditions vary from those used to generate the prototypes. When the variants of prototypes contain strongly overlapped signals with unknown relative peak intensities compared to the prototypes, phase mapping can only be solved (by humans or AI) through reasoning about prior knowledge based on thermodynamics. These “rules” are more nuanced than those of Sudoku and are described in detail in **Supplementary Methods**. Briefly, when combining 3 elements, the number of phases that can appear in an input pattern is at most 3, and is at most 2 if the composition is in a region that exhibits alloying. This latter rule requires consideration of the composition graph of the input XRD patterns, which is also used to enforce a rule wherein each set of prototypes can only appear in compositions that are connected in the graph.

State-of-the-art approaches for phase mapping are unsupervised methods based on matrix factorization, and have incorporated thermodynamic rules to different extents, including analysis of the composition graph<sup>26</sup>, integration of demixing with clustering<sup>27</sup>, and recent work that interleaves matrix factorization with constraint optimization to enforce all the thermodynamic rules<sup>28</sup>. Nev-

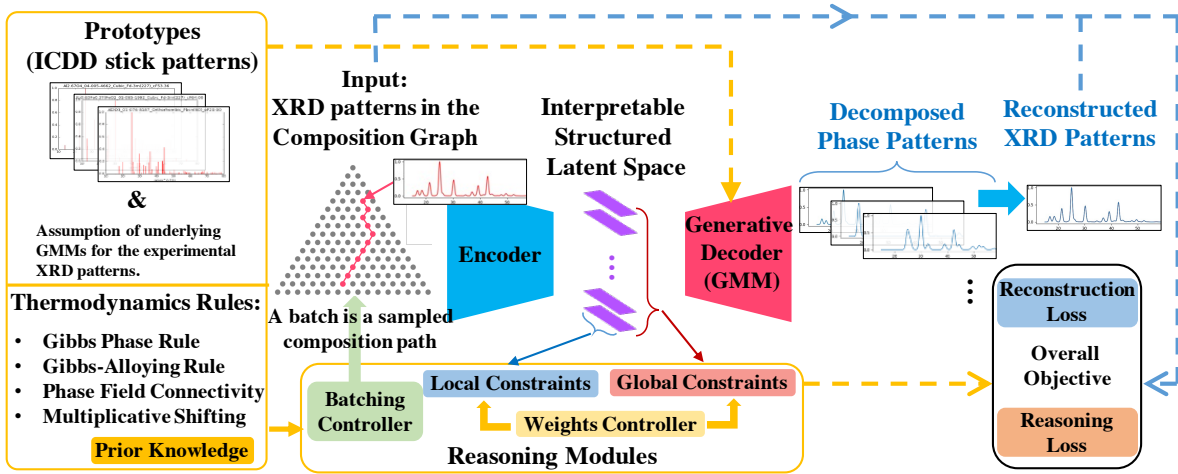
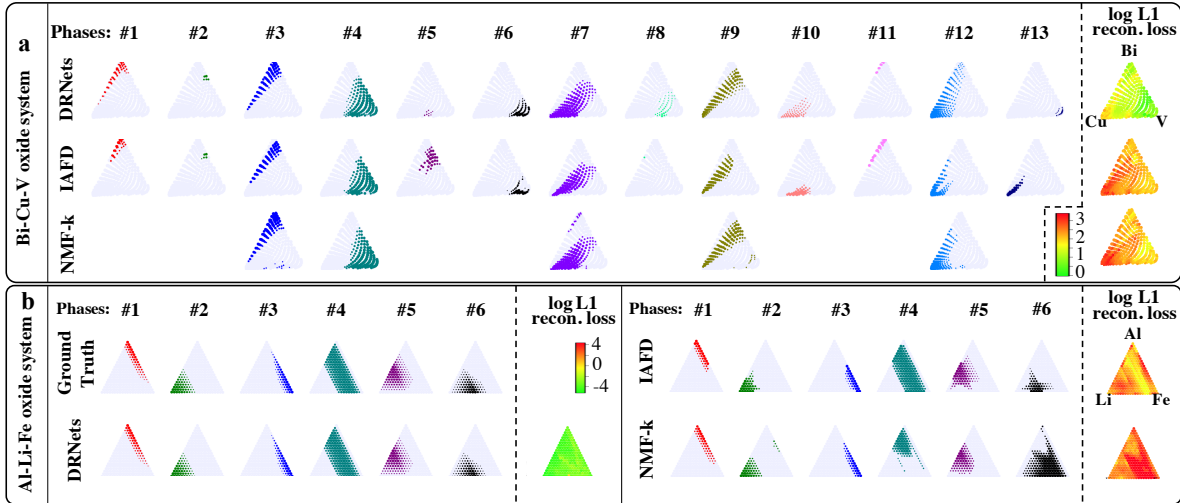
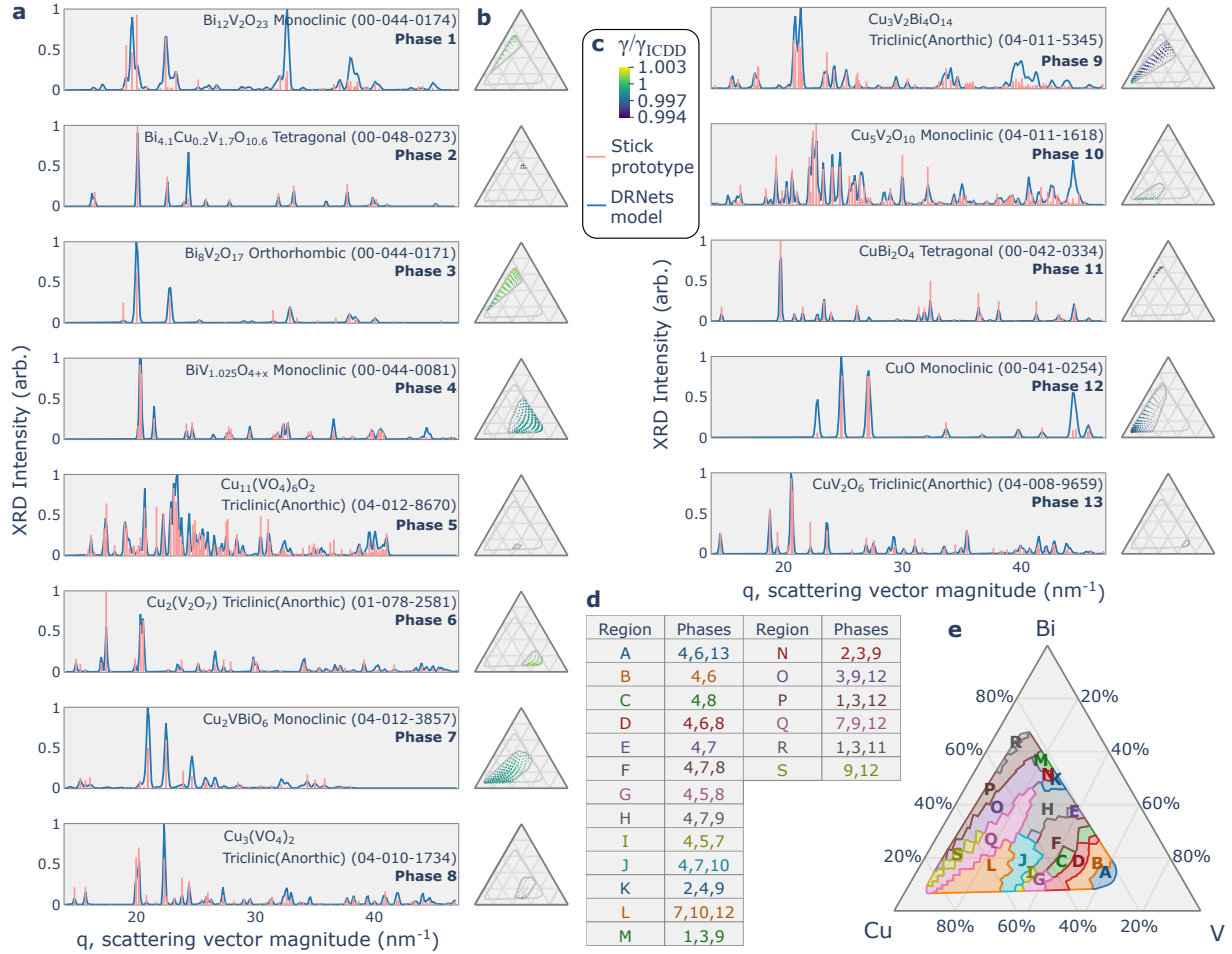


Figure 3: **DRNets for Crystal-Structure Phase Mapping** DRNets perform end-to-end deep reasoning by encoding a latent space that is used by a generative decoder to reconstruct the XRD measurements. The input is the XRD patterns, each resulting from a mixture of phases, and the output is the decomposed pure phase patterns and the reconstructed mixture. The encoder is composed of four 3-layer-fully-connected networks. The structured latent encoding is constrained to adhere to thermodynamic rules by the reasoning module. Prior knowledge also includes prototype stick patterns, which are used by the generative decoder, a Gaussian mixture model, to generate the corresponding possible phase patterns in the reconstructed XRD measurement. An overall objective combines responses from the generative decoder, for pattern reconstruction, and the reasoning module, for applying thermodynamic rules, which is optimized using constraint-aware stochastic gradient descent.

ertheless, these approaches only use known prototype patterns to post-process demixing results, resulting in a more ill-conditioned demixing. In contrast, DRNets provide the first framework that integrates enforcement of thermodynamic rules with reasoning about the prototypes, solving previously unsolvable phase mapping problems. The DRNets for crystal-structure phase-mapping (Fig. 3) seamlessly integrate demixing and reconstruction of XRD patterns by coupling an encoder with four 3-layer-fully-connected neural networks, which produces a two-part structured latent space (Fig. 2b), to a generative Gaussian Mixture model that incorporates prior knowledge about prototype phases, and by generating XRD patterns based on mixtures of modified versions of prototypes. The modifications include peak intensity modulation and alloying-based peak shifting; the semantic representation of the prototype-modification parameters in the latent space enables DRNets to learn their optimal values under guidance from priors that are parameterized by prior knowledge of the maximum extent of prototype modification. The latent variables also enable expression of thermodynamic rules with entropy-based functions, which are imposed with a batching sampling strategy to tackle the combinatorics of all-sample thermodynamic constraints (Fig. 3). DRNets are optimized with the hybrid objective of reconstructing measured patterns and enforcing thermodynamic rules, as detailed in [Methods](#).



**Figure 4: Comparison of the activation maps produced by DRNets with other unsupervised approaches for the Bi-Cu-V oxide and Al-Li-Fe oxide systems.** (a) The activation map of the 307 composition points of the Bi-Cu-V oxide system for each of the 13 phases identified by DRNets is shown, with comparison to IAFD and NMF-k solutions (see Extended Data Fig. 5), demonstrating their ability to capture some aspects of the phase activations while misrepresenting or omitting several phases that are key to generating a meaningful phase diagram. The reconstruction loss for each pattern is also shown demonstrating that only through correct identification of the phases can the XRD dataset be fully explained. In (b), we highlight the performance of the different methods on the synthetically generated Al-Li-Fe oxide system (231 composition points), which has ground truth: DRNets are the only system that nearly perfectly identifies the phases present in every XRD pattern. The different methods share a common color scale for reconstruction loss in each system, and the elemental labels for the composition triangle are only provided once per system. See further details in Fig. 6a.



**Figure 5: DRNets' solution for the Bi-Cu-V oxide system.** **a.** The 13 demixed crystal phases for the 307 XRD measurements of the Bi-Cu-V oxide system (each plot includes the signal for the recognized phase and the corresponding ICDD stick pattern). **b.** DRNets' phase concentration maps for each of the phases, where point sizes are proportional to their estimated phase concentrations and heatmap denotes estimated shifting (alloying). **c.** Shows the universal legend for the 13 phases in **a** and **b**, where  $\gamma$  is the average lattice constant. **d.** Table of all phase mixtures in the DRNets solution. **e.** DRNets' crystal phase map for the Bi-Cu-V-O system with phase fields labeled according to **d**.

Since ground truth is unavailable for previously-unsolvable experimental phase mapping datasets, we first compare DRNets to state of the art methods NMF-k<sup>27</sup> and IAFD<sup>28</sup> using a synthetic benchmark dataset (with ground truth), based on the Al-Li-Fe oxide system,<sup>27;34</sup> which contains 6 phases in 15 unique combinations (from 159 prototypes) with substantial alloying. DRNets outperform NMF-k and IAFD in a variety of metrics. We also considered a recently proposed supervised algorithm<sup>31</sup> in which a deep neural network, trained using XRD patterns simulated from prototypes of known phases, directly predicts the phases present in a given XRD pattern. While such an approach can be effective for complementing human expertise for a single XRD pattern, it performed poorly on a complex system such as the benchmark Al-Li-Fe oxide system (phase identification accuracy around 1%), which exposes the limitations of a purely simulation-based supervised approach for handling the combinatorics of phase mapping (details in [Supplementary Methods](#)). In contrast, the DRNets approach is the only one that perfectly identifies the phases present in every XRD pattern and learns the phase-pure patterns (Extended Data Fig. 5). The DRNets model outperforms other algorithms in a variety of other metrics (See Fig. 4b and Fig. 6a). In an ablation study we show that DRNets need around 150 input XRD patterns to approach the ground truth solution in the Al-Li-Fe oxide system (Fig. 6b). This study highlights the importance of the data-driven learning of the shared parameters of the demixing task across multiple XRD patterns, which enables each pattern to be demixed in a manner that is often not possible with single isolated XRD patterns. Nevertheless, DRNets' data requirements (hundreds of data points) are considerably smaller than those of standard deep learning approaches (hundreds of thousands of data points).

To represent unsolved experimental datasets, we use the Bi-Cu-V oxide system where manual analysis was found to be particularly ineffective to solve the system due to the complexity of the alloying in the set of 307 XRD patterns, as well as strong overlap of signals in the 100 prototypes (Fig. 1a-f and Fig. 5). DRNets identified 13 phases in 19 unique mixtures (Fig. 4a and Fig. 5), and the presence of each phase was verified by manual analysis using standard practices based on absence of missing peaks and inability to explain the signal with other prototypes. We note that in practice verifying a solution is easier than producing it. For example, visual inspection of Fig. 5 reveals the excellent agreement between the stick prototype and the demixed DRNets model for each phase, and this analysis was extended to patterns from the experimental dataset that were chosen based on high activation of each phase and each phase mixture, a manual validation based on representative patterns from the solution. To assess the extent by which learning the pattern interrelationships is critical for solving the Bi-Cu-V oxide system, we consider a model analogous to DRNets for demixing a single XRD pattern in isolation. This model identifies the same phases as DRNets for only 27% of the patterns, highlighting that the nuanced phase behavior of this system can only be resolved through combinatorial experimentation combined with reasoning about the underlying thermodynamic constraints to learn the shared parameters across multiple XRD patterns. As shown in Fig. 4a, the DRNets activation maps (the amount of each demixed pattern in each input XRD pattern) for 5-8 of the phases are poorly reproduced by NMF-k and IAFD. The demixed patterns in these solutions, which are intended to be phase-pure patterns, contain mixtures with the less-commonly-occurring phases, making the minor phases undiscoverable by these methods

and hampering inference of scientific knowledge from the phase mapping solution. The “fidelity loss” quantifies the deviation of the demixed patterns from its closest prototype (see [Supplementary Methods](#)), and the lack of phase purity in the demixed NMF-k and IAFD solutions contribute to their substantial fidelity loss compared to DRNets (Fig. 6a). The low fidelity loss of the DRNets solution is commensurate with the manual verification of the presence of phases identified by DRNets, although this analysis does not preclude the false negative detection of a phase in any given XRD pattern. Such an imperfection in the solution would give rise to a reconstruction error, and Fig. 6a demonstrates that the reconstruction loss for DRNets is substantially lower than those of other methods, indicating that false negative phase detection is not a major issue in the DRNets solution. Substantial reconstruction loss can also occur if the experimental data contains a phase that is missing from the set of prototypes, which would prompt an investigation of phase discovery, as discussed further in the [Supplementary Methods](#). The activation accuracy metric assesses the phase concentrations in each measured pattern but can be quantified only when ground truth is available, as in the synthetic dataset where DRNets substantially outperform other methods. Datasets with poor signal-to-noise ratio and/or XRD peak widths that do not enable unambiguous phase identification can result in different solutions that still satisfy thermodynamic rules and reconstruct the source data<sup>28</sup>. Evaluating the stability of DRNets’ phase mapping solutions with active feedback from experiments is an interesting avenue that we are pursuing.

Informed by the DRNets solution, analysis of the photo-oxidation of water (a critically limiting component of solar fuels technology) revealed that a 3-phase mixture (alloy variants of BiVO<sub>4</sub>, Cu<sub>2</sub>BiVO<sub>6</sub> and Cu<sub>3</sub>(VO<sub>4</sub>)<sub>2</sub>) outperforms the standard monoclinic BiVO<sub>4</sub> material, defying the conventional wisdom that phase mixtures are deleterious to photoactivity (Extended Data Fig. 6). DRNets’ performance for phase mapping is emblematic of how seamlessly combining deep learning with reasoning about prior scientific knowledge can automate the interpretation of scientific data and accelerate knowledge discovery.

	Methods	# of phases	Activation Accuracy	Reconstruction Loss (L1)	Reconstruction Loss (L2)	Gibbs	Gibbs Alloy	Phase Field Connectivity	Fidelity Loss
Al-Li-Fe	DRNets	6	100%	0.038	<0.001	100%	100%	100%	<0.001
	IAFD	6	80.6%	6.921	0.778	100%	100%	100%	11.920
	NMF-k (k=6)	6	63.1%	29.805	7.169	93.9%	87.0%	71.0%	46.156
Bi-Cu-V	DRNets	13	N/A	3.916	0.268	100%	100%	100%	0.482
	IAFD	13	N/A	11.254	1.781	100%	100%	100%	55.571
	NMF-k (k=5)	5	N/A	10.453	1.577	99.7%	99.7%	48%	48.674
	NMF-k (k=13)	13	N/A	11.258	1.399	52.4%	52.4%	86.9%	68.471

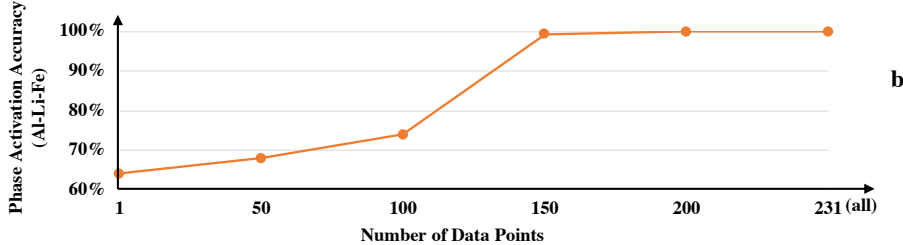


Figure 6: **a. Comparison of different performance metrics for different methods for the Al-Li-Fe oxide system and the Bi-Cu-V oxide system.** Gibbs, Gibbs alloy, and phase connectivity metrics denote the proportion of samples satisfying the Gibbs, Gibbs alloy, and phase connectivity rules; the phase fidelity loss (Fidelity Loss) denotes how well the discovered phase patterns match the ground truth (the lower the better ([See Supplementary Methods](#))). For the Al-Li-Fe oxide system, the DRNets solution has 6 phases, which matches ground truth, and this known number of phases was applied to IAFD and NMF-k. For the Bi-Cu-V oxide system, both DRNets' and IAFD's solutions have 13 phases (the number of phases was specified for IAFD but not DRNets) while NMF-k has 5 phases. Nevertheless, we also run NMF-k with 13 phases following the verification of the presence of the 13 phases from the DRNets solution. Note that, there is no ground truth for the Bi-Cu-V oxide system, therefore the activation accuracy is not applicable (N/A). The results indicate that DRNets perform substantially better than IAFD and NMF-k for all the metrics on both systems (Additional details in [Supplementary Methods](#)). **b. The performance of DRNets on Crystal-Structure Phase Mapping (Al-Li-Fe oxide system) with different number of XRD data points.** Learning over multiple XRD patterns within a composition system plays an important role for DRNets to solve crystal-structure phase mapping problem. As shown in the plot, for Al-Li-Fe oxide system, DRNets can almost perfectly recover the phase activation of XRD patterns when it learns via demixing of a collection of at least 150 XRD patterns.

## Discussion

A central tenet of the scientific process is the interpretation of data in the context of a rich body of scientific knowledge. However, the efficient integration of complex prior knowledge into machine learning approaches has been an open challenge in AI. DRNets provide a general modular framework for incorporating prior knowledge that can be customized to effectively tackle unsupervised pattern demixing tasks. Herein we provide an in-depth description of the application of DRNets to a scientific application, crystal-structure phase mapping, a fundamental long-standing challenge in materials science. We also illustrate the application of DRNets to a Sudoku demixing task, which is

facilitated by the availability of benchmark data for algorithm comparisons and ablations studies. In the DRNets framework, an *interpretable* structured latent space is crucial for the incorporation of background knowledge (see Fig. 2 and Extended data Fig. 7). *The semantics of the latent space emerges during the optimization process as the result of the interplay among the encoder, the generative decoder, the reasoning module, and (unlabeled) data.* We showed the effectiveness of our approach, such as for crystal-phase mapping, where DRNets significantly outperformed previous approaches and solved previously unsolved complex chemical systems, aiding the discovery of solar-fuels materials. Intuitively, the strong prior knowledge injected via the fixed generative decoder and reasoning constraints, combined with the data, constrain the optimization process to enforce the intended semantics of the latent space. As our Sudoku ablation studies show, if we either replace the fixed cGAN with a (weaker) standard learnable decoder, without prior knowledge about single digits, or remove the reasoning modules, the optimization process can no longer find the right semantics for the latent space, and the digit and Sudoku accuracy deteriorate significantly. Data are critical, as they ultimately determine the semantics of the latent space, and DRNets clearly benefit from learning across multiple (unlabeled) instances. Nevertheless, somewhat surprisingly, the amount of unlabeled data required in DRNets for both the Sudoku and crystal-structure phase mapping applications is considerably more modest than in standard supervised deep learning settings.

The DRNets framework is general and modular and can be adapted to other de-mixing and unsupervised tasks for which domain rules and pattern prototypes or generative models are available. In addition, prior knowledge can also increase interpretability and boost performance of supervised models, another research directions for DRNets. In fact, some of the ideas in DRNets were inspired by our work in the context of supervised learning on multi-label classification and in particular deep-learning-based joint species distribution models (JSDMs)<sup>35</sup> that integrate prior ecological knowledge and species observational training data from the eBird citizen science program.<sup>36</sup> The need to capture and interpret interactions between species and their local environments as well as interactions among different species, which are core questions in ecology and conservation,<sup>37</sup> was the initial motivation and inspiration for the semantically meaningful structured latent-space in the DRNets framework.<sup>35</sup> We anticipate that these concepts will extend to other tasks, for example, materials science tasks beyond phase mapping, such as property prediction. The construction of a latent space with intended semantics can not only enable constraint reasoning, as demonstrated in the present work, but also facilitate transfer learning wherein relationships among composition, structure, and some types of properties can be used to learn relationships for other types of properties. Such concepts extend the purview of prior knowledge from the rules and prototypes employed in the present work to rules, surrogate models, etc. from ancillary domains. More generally, research on incorporating neural network-based learning with symbolic knowledge representation and logical reasoning is an important next frontier in AI/ML research.<sup>19</sup> The DRNets framework represents a step in that direction, providing a modular end-to-end framework that can be customized for a range of tasks that require the combination of learning and reasoning, which are pervasive across a variety of application domains.

## Methods

**Mathematical formulation of DRNets.** In order to produce a DRNets encoding for a given task, we start by formulating the task as a data-driven constrained optimization problem, which is then transformed through a sequence of steps into a data-driven unconstrained optimization problem amenable to end-to-end optimization via state-of-the-art deep learning technology (Extended Data Fig. 1a). More formally, the formulation of a DRNets task as a data-driven constrained optimization problems is as follows:

$$\min_{\theta} \frac{1}{N} \sum_{i=1}^N \mathcal{L}(G(\phi_{\theta}(\mathbf{x}_i)), \mathbf{t}_i) \quad \text{subject to: } \phi_{\theta}(\mathbf{x}_i) \in \Omega^{\text{local}} \text{ and } (\phi_{\theta}(\mathbf{x}_1), \dots, \phi_{\theta}(\mathbf{x}_N)) \in \Omega^{\text{global}}$$

where  $\phi_{\theta}(\mathbf{x}_i) := (\mathbf{z}_{i,1}, \dots, \mathbf{z}_{i,m}, \mathbf{e}_{i,1}, \dots, \mathbf{e}_{i,m})$  (1)

In this formulation,  $N$  is the number of input data points,  $m$  is the number of possible single patterns,  $\mathbf{x}_i \in R^n$  is the  $i$ -th  $n$ -dimensional input data point,  $\mathbf{t}_i$  is the corresponding targeted output, which is in general the input  $\mathbf{x}_i$  in unsupervised cases,  $\phi_{\theta}(\mathbf{x}_i) := (\mathbf{z}_{i,1}, \dots, \mathbf{z}_{i,m}, \mathbf{e}_{i,1}, \dots, \mathbf{e}_{i,m})$  is the latent space of DRNets for data point  $\mathbf{x}_i$ , a function of the encoder  $\phi$  parameterized by  $\theta$ , typically a neural network.  $\mathbf{z}_{i,j}$  and  $\mathbf{e}_{i,j}$  are the *shape* and *probability embeddings* of the possible pattern- $j$  at data point  $\mathbf{x}_i$  indicating its shape and probability.  $G(\cdot)$  is the generative decoder which involves a fixed pre-trained or parametric generative model that generates single patterns from shape embeddings  $\mathbf{z}_{i,j}$  and a process that mixes the generated single patterns factoring in their probabilities.  $\mathcal{L}(\cdot, \cdot)$  is the loss function, which evaluates the loss between the output of the generative decoder and the target  $\mathbf{t}_i$ ,  $\Omega^{\text{local}}$  and  $\Omega^{\text{global}}$  are the constrained spaces w.r.t. a single input data point and several input data points, respectively. Note that constraints can involve several (potentially all) data points: e.g., in Sudoku, all digits should form a valid Sudoku and in crystal-structure-phase-mapping, all data points in a composition graph should form a valid phase diagram. Thus, we specify local and global constraints in DRNets – local constraints only involve a single input data point whereas global constraints involve several input data points, and they are optimized using different strategies. For the Multi-MNIST-Sudoku DRNets,  $\phi_{\theta}(\cdot)$  is composed of two ResNet-18. The generative model in  $G(\cdot)$  is a pre-trained conditional GAN<sup>38</sup> using hand-written digits; for the Crystal-Structure-Phase-Mapping DRNets,  $\phi_{\theta}(\cdot)$  is composed of four 3-layer-fully-connected networks and  $G(\cdot)$  involves a Gaussian Mixture model. Below we provide details for each specific application.

Finally, we note that we refer to *data-driven* constrained/unconstrained optimization problems to highlight the fact that even though we assign an interpretation to the structured latent-space produced by the encoder,  $\phi_{\theta}(\mathbf{x}_i)$ , the latent-space semantics are ultimately determined by the data. (See also Extended Data Fig. 7 for a summary of the different components of DRNets for the different tasks.)

**Transformation flow for DRNets.** Solving the constrained optimization problem in equation (1) directly is challenging since the objective function in general involves deep neural networks, which are highly non-linear and non-convex, and prior knowledge often involves combinatorial constraints, which cannot be directly encoded in a standard deep learning framework. Extended

Data Fig. 1a depicts how we reduce the above constraint optimization problem into DRNets. In particular, we use Lagrangean relaxation to approximate the constrained optimization problem (equation 1) with an unconstrained optimization problem, moving the constraints to the objective function with associate penalty weights:

$$\min_{\theta} \frac{1}{N} \sum_{i=1}^N \mathcal{L}(G(\phi_{\theta}(\mathbf{x}_i)), \mathbf{t}_i) + \lambda^l \psi^l(\phi_{\theta}(\mathbf{x}_i)) + \sum_{j=1}^{N_g} \lambda_j^g \psi_j^g(\{\phi_{\theta}(\mathbf{x}_k) | k \in S_j\})$$

where  $\phi_{\theta}(\mathbf{x}_i) := (\mathbf{z}_{i,1}, \dots, \mathbf{z}_{i,m}, \mathbf{e}_{i,1}, \dots, \mathbf{e}_{i,m})$  (2)

Herein,  $N_g$  denotes the number of global constraints,  $S_j$  denotes the set of indices w.r.t. the data points involved in the  $j$ -th global constraint, and  $\psi^l, \psi_j^g$  denote the penalty functions for local constraints and global constraints, respectively, along with their corresponding penalty weights  $\lambda^l$  and  $\lambda_j^g$ . As outlined in Extended Data Fig. 1a, we employ two mechanisms to tackle the above unconstrained optimization task: (1) *continuous relaxations* of constraints with discrete variables and (2) *constraint-aware stochastic gradient descent* to tackle global penalty functions, for the different types of combinatorial constraints.

**Continuous Relaxations:** Prior knowledge often involves combinatorial constraints with discrete variables that are difficult to optimize in an end-to-end manner using gradient-based methods. Therefore, we need to design proper continuous relaxations for discrete constraints to make the overall objective function differentiable. Many approaches have been used to handle continuous relaxations of discrete constraints<sup>39;40</sup>. We apply a group of entropy-based continuous relaxations to encode general discrete constraints such as sparsity, cardinality, and All-Different constraints. We construct continuous relaxations based on probabilistic modelling of discrete variables, where we model a probability distribution over all possible values for each discrete variable. For example, in Multi-MNIST-Sudoku, a way of encoding the possible two digits in the cell indicated by data point  $x_i$  (one from  $\{1\dots4\}$  and the other from  $\{5\dots8\}$ ), is to use 8 binary variables  $e_{i,j} \in \{0, 1\}$ , while requiring  $\sum_{j=1}^4 e_{i,j} = 1$  and  $\sum_{j=5}^8 e_{i,j} = 1$ . In DRNets, we model probability distribution  $P_i$  and  $Q_i$  over digits 1 to 4 and 5 to 8 respectively:  $P_{i,j}, j=1\dots4$  and  $Q_{i,j}, j=1\dots4$  denote the probability of digit  $j$  and the probability of digit  $j+4$ , respectively. We approximate the cardinality constraint of  $e_{i,j}$  by minimizing the entropy of  $P_i$  and  $Q_i$ , which encourages  $P_i$  and  $Q_i$  to collapse to one value. See details concerning relaxations for other constraints in Extended Data Fig.1b and [Supplementary Methods](#).

**Constraint-Aware Stochastic Gradient Descent:** We developed a variant of the standard SGD method that we refer to as constraint-aware SGD, which batches data points involved in the same global constraint together, conceptually similar to the optimization process in GraphRNN<sup>41</sup>, to tackle the optimization of global penalty functions  $\psi_j^g(\{\phi_{\theta}(\mathbf{x}_k) | k \in S_j\})$ , which involve several (potentially all) data points. We define a *constraint graph*, an undirected graph in which each data point forms a vertex and two data points are linked if they are in the same global constraint. Constraint-aware SGD batches data points from the randomly sampled (maximal) connected components in the *constraint graph*, and optimizes the objective function w.r.t. the subset of global constraints concerning those data points and the associated local constraints. For example,

---

**Algorithm 1** Constraint-aware stochastic gradient descent optimization of deep reasoning networks.

---

**Require:** **(i)** Data points  $\{x_i\}_{i=1}^N$ . **(ii)** Constraint graph. **(iii)** Penalty functions  $\psi^l(\cdot)$  and  $\psi_j^g(\cdot)$  for the local and the global constraints. **(iv)** Pre-trained or parametric generative decoder  $G(\cdot)$ .

- 1: Initialize the penalty weights  $\lambda^l$ ,  $\lambda_j^g$  and thresholds for all constraints.
- 2: **for** number of optimization iterations **do**
- 3:   Batch data points  $\{\mathbf{x}_1, \dots, \mathbf{x}_m\}$  from the sampled (maximal) connected components.
- 4:   Collect the global penalty functions  $\{\psi_j^g(\cdot)\}_{j=1}^M$  concerning those data points.
- 5:   Compute the latent space  $\{\phi_\theta(\mathbf{x}_1), \dots, \phi_\theta(\mathbf{x}_m)\}$  from the encoder.
- 6:   Adjust the penalty weights  $\lambda^l$ ,  $\lambda_j^g$  and thresholds accordingly.
- 7:   minimize  $\frac{1}{m} \left( \sum_{i=1}^m \mathcal{L}(G(\phi_\theta(\mathbf{x}_i)), \mathbf{x}_i) + \lambda^l \psi^l(\phi_\theta(\mathbf{x}_i)) \right) + \sum_{j=1}^M \lambda_j^g \psi_j^g(\{\phi_\theta(\mathbf{x}_k) | k \in S_j\})$  using any standard gradient-based optimization method and update the parameters  $\theta$ .
- 8: **end for**

---

in Multi-MNIST-Sudoku, the data points (cells) in each overlapping Sudoku form a maximal connected component in the *constraint graph*, so we batch the data points from several randomly sampled overlapping Sudokus and optimize the All-Different constraints (global) as well as the cardinality constraints (local) within them. However, in Crystal-Structure Phase Mapping, the maximal connected component becomes too large to batch together, due to the constraints (*phase field connectivity* and *Gibbs-alloying rule*) concerning all data points in the composition graph. Thus, we instead only batch a subset (still a connected component) of the maximal connected component – e.g., a path in the composition graph, and optimize the objective function that only concerns constraints within the subset (along the path). By iteratively solving sampled local structures of the "large" maximal component, we cost-efficiently approximate the entire global constraint. For efficiency, DRNets solve all instances together using constraint-aware SGD (see Algorithm 1)

Moreover, for optimizing the overall objective, constraint-aware SGD dynamically adjusts the thresholds and the weights of constraints according to their satisfiability, which can involve non-differentiable functions. Specifically, we initialize the penalty weights and thresholds of constraints for penalty functions using hyper-parameters. During optimization DRNets keep track of the satisfiability of constraints (this step could involve non-differentiable functions) and adjust the penalty weights and thresholds based on their satisfiability. For example, in crystal-structure phase mapping, we use the k-sparsity constraint to implement the Gibbs rule (the number of phases than can coexist is at most 3 in a ternary chemical system) and the Gibbs-Alloy rule (the max phase count decreases by 1 if "alloying" occurs) in DRNets. The threshold  $c$  of k-sparsity is initialized as  $\log 3$  (Gibbs rule), which is the entropy when the probability mass is evenly distributed among 3 phases. During the optimization of DRNets, if "alloying" occurs (by checking the phase shifting ratio between adjacent data points), DRNets decrease the max phase count from 3 to 2 and adjust the threshold  $c$  from  $\log 3$  to  $\log 2$  (Gibbs-Alloy rule) accordingly. Moreover, note that even if we optimize the penalty function ( $H(P_M)$ ) to be equal or smaller than  $\log k$  ( $k$  is 2 or 3), it could be the case that there are more than  $k$  phases with positive probability mass ( $> 0.01$ ) and their probability mass may not be evenly distributed, which means the k-sparsity is still not satisfied. Thus, DRNets keep tracking the satisfiability of k-sparsity constraint: if the entropy is already below

the current threshold (e.g.,  $\log k$ ) and there are still more than  $k$  phases with probability mass more than  $\epsilon$  (0.01), we decrease the threshold  $c$  to keep enforcing the model to minimize the entropy until reaching the  $k$ -sparsity.

**Computational details:** All the experiments are performed on one NVIDIA Tesla V100 GPU with 16GB memory. For the training process of our DRNets, we select a learning rate in  $\{0.0001, 0.0005, 0.001\}$  with Adam optimizer<sup>42</sup>, for all the experiments. For baseline models, we followed their original configurations and further fine-tuned their hyper-parameters to saturate their performance on our tasks.

**Acknowledgements** The development of DRNets was supported by NSF awards CCF-1522054 (Expeditions in computing), and CNS-1059284 (Infrastructure). DRNets for phase mapping and corresponding experimental work were also supported by AFOSR Multidisciplinary University Research Initiatives (MURI) Program FA9550-18-1-0136, ARO awards W911NF-14-1-0498 and W911NF-17-1-0187, and an award from the Toyota Research Institute. Solar fuels experiments were supported by US DOE Award No. DE-SC0004993 and solar photochemistry analysis in the context of the DRNets solution was supported by US DOE Award No. DE-SC0020383. Use of SSRL is supported by DOE Contract No. DE-AC02-76SF00515. The authors also thank Junwen Bai for assistance with running the IAFD baseline, Aniketa Shinde for photoelectrochemistry experiments, and Rich Berstein for assistance with figure generation.

**Competing Interests** The authors declare that they have no competing financial interests.

**Data availability** MNIST-Sudoku and crystal-structure mapping data will be available for download from: Data provided in zip file with supplementary files. Please do not distribute it (confidential). GitHub link to be provided if/when manuscript accepted.

**Contributions** C.P.G. conceived and managed the overall study. J.M.G. and C.P.G. conceived and managed the crystal-structure phase mapping project. D.C. and C.P.G. conceived the MNIST-SUDOKU project. D.C. and C.P.G. conceptualized Deep Reasoning Nets. D.C. developed and implemented DRNets, in particular, DRNets for MVP, MNIST-Sudoku, and Crystal-Structure Phase mapping. Y.B. performed the large-scale experiments, assisted on implementing DRNets for MNIST-Sudoku, and baseline comparisons for MNIST-Sudoku. S.A. performed background subtraction for the Bi-Cu-V-O system. W.Z. implemented baselines for crystal-structure phase mapping and assisted on generating MNIST-Sudoku data. L.Z. and D.G. generated phase mapping datasets and interpreted/validated solutions. C.P.G., D.C., and J.M.G. were the main authors of the manuscript with contributions from B.S. and R.B.v.D. and comments from all authors.

**Code availability** All relevant code will be available from: Code provided in zip file with supplementary file. Please do not distribute it (confidential). GitHub link to be provided with final version of manuscript.

**Correspondence** Correspondence and requests for materials should be addressed to: C.P.G. (gomes@cs.cornell.edu) and J.M.G. (gregoire@caltech.edu).

## References

1. Jelena Stajic, Richard Stone, Gilbert Chin, and Brad Wible. Rise of the Machines. *Science*, 349(6245):248–249, July 2015. Publisher: American Association for the Advancement of Science Section: Introduction to special issue.
2. Christian Szegedy, Wei Liu, Yangqing Jia, Pierre Sermanet, Scott Reed, Dragomir Anguelov, Dumitru Erhan, Vincent Vanhoucke, and Andrew Rabinovich. Going deeper with convolutions. In *Proceedings of the IEEE conference on computer vision and pattern recognition*, pages 1–9, 2015.
3. Yaniv Taigman, Ming Yang, Marc’Aurelio Ranzato, and Lior Wolf. Deepface: Closing the gap

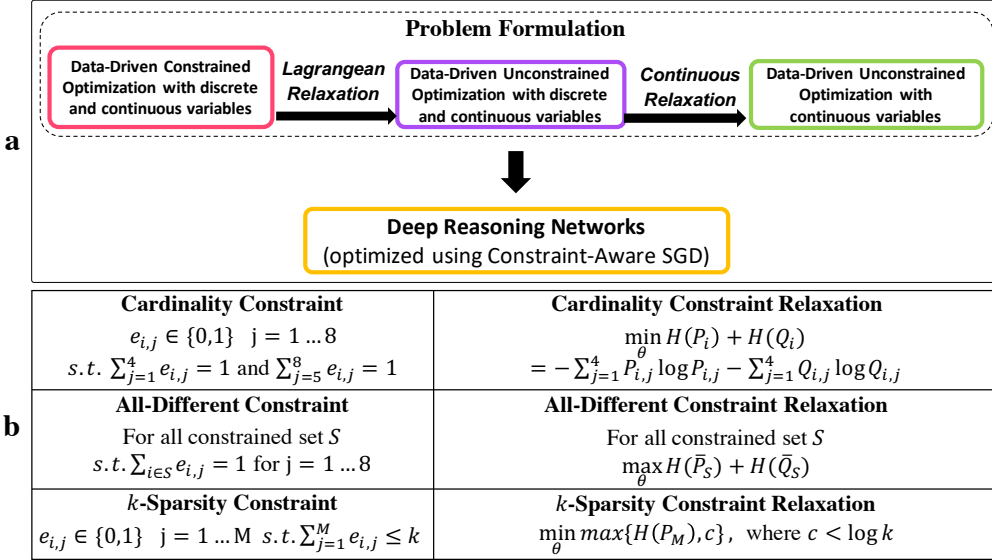
- to human-level performance in face verification. In *Proceedings of the IEEE conference on computer vision and pattern recognition*, pages 1701–1708, 2014.
4. Alex Graves, Abdel-rahman Mohamed, and Geoffrey Hinton. Speech recognition with deep recurrent neural networks. In *2013 IEEE international conference on acoustics, speech and signal processing*, pages 6645–6649. IEEE, 2013.
  5. Yolanda Gil, Mark Greaves, James Hendor, and Haym Hirsh. Amplify scientific discovery with artificial intelligence. *Science*, 346(6206):171–172, 2014.
  6. Philip Ball. Learning from the big picture. *Nature materials*, 17(12):1062–1062, 2018.
  7. Daniel P Tabor, Loïc M Roch, Semion K Saikin, Christoph Kreisbeck, Dennis Sheberla, Joseph H Montoya, Shyam Dwarakanath, Muratahan Aykol, Carlos Ortiz, Hermann Tribukait, et al. Accelerating the discovery of materials for clean energy in the era of smart automation. *Nature Reviews Materials*, 3(5):5–20, 2018.
  8. Benjamin Sanchez-Lengeling and Alán Aspuru-Guzik. Inverse molecular design using machine learning: Generative models for matter engineering. *Science*, 361(6400):360–365, 2018.
  9. Shijing Sun, Noor T. P. Hartono, Zekun D. Ren, Felipe Oviedo, Antonio M. Buscemi, Mariya Layurova, De Xin Chen, Tofunmi Ogunfunmi, Janak Thapa, Savitha Ramasamy, Charles Settens, Brian L. DeCost, Aaron G. Kusne, Zhe Liu, Siyu I. P. Tian, Ian Marius Peters, Juan-Pablo Correa-Baena, and Tonio Buonassisi. Accelerated Development of Perovskite-Inspired Materials via High-Throughput Synthesis and Machine-Learning Diagnosis. *Joule*, 3(6):1437–1451, June 2019.
  10. A. Gilad Kusne, Heshan Yu, Changming Wu, Huairuo Zhang, Jason Hattrick-Simpers, Brian DeCost, Suchismita Sarker, Corey Oses, Cormac Toher, Stefano Curtarolo, Albert V. Davydov, Ritesh Agarwal, Leonid A. Bendersky, Mo Li, Apurva Mehta, and Ichiro Takeuchi. On-the-fly closed-loop materials discovery via Bayesian active learning. *Nature Communications*, 11(1):5966, November 2020.
  11. Yann LeCun, Yoshua Bengio, and Geoffrey Hinton. Deep learning. *Nature*, 521(7553):436–444, 2015.
  12. Di Chen, Yiwei Bai, Wenting Zhao, Sebastian Ament, John Gregoire, and Carla Gomes. Deep reasoning networks for unsupervised pattern de-mixing with constraint reasoning. In *Proceedings of the 37th international conference on machine learning (ICML-2020)*, 2020.
  13. Takayuki Yato and Takahiro Seta. Complexity and completeness of finding another solution and its application to puzzles. *IEICE transactions on fundamentals of electronics, communications and computer sciences*, 86(5):1052–1060, 2003.
  14. Francesca Rossi, Peter Van Beek, and Toby Walsh. *Handbook of constraint programming*. Elsevier, 2006.

15. Simon Gravel and Veit Elser. Divide and concur: A general approach to constraint satisfaction. *Physical Review E*, 78(3):036706, September 2008.
16. V. Elser, I. Rankenburg, and P. Thibault. Searching with iterated maps. *Proceedings of the National Academy of Sciences*, 104(2):418–423, January 2007. Publisher: National Academy of Sciences Section: Physical Sciences.
17. Ronan LeBras, Theodoros Damoulas, John M Gregoire, Ashish Sabharwal, Carla P Gomes, and R Bruce Van Dover. Constraint reasoning and kernel clustering for pattern decomposition with scaling. In *International Conference on Principles and Practice of Constraint Programming*, pages 508–522. Springer, 2011.
18. Note. We refer to a setting as unsupervised when no labeled training data are available for the target output. For example, Multi-MNIST-Sudoku DRNets are unsupervised since they don't have access to labeled mixed-digit training data.
19. Artur d'Avila Garcez and Luis C. Lamb. Neurosymbolic AI: The 3rd wave, 2020.
20. Yann LeCun, Léon Bottou, Yoshua Bengio, Patrick Haffner, et al. Gradient-based learning applied to document recognition. *Proceedings of the IEEE*, 86(11):2278–2324, 1998.
21. Gregory Cohen, Saeed Afshar, Jonathan Tapson, and André van Schaik. Emnist: an extension of mnist to handwritten letters (2017). *arXiv preprint arXiv:1702.05373*, 2017.
22. Sara Sabour, Nicholas Frosst, and Geoffrey E Hinton. Dynamic routing between capsules. In *Advances in neural information processing systems*, pages 3856–3866, 2017.
23. Kaiming He, Xiangyu Zhang, Shaoqing Ren, and Jian Sun. Deep residual learning for image recognition. In *Proceedings of the IEEE conference on computer vision and pattern recognition*, pages 770–778, 2016.
24. Alfred Ludwig. Discovery of new materials using combinatorial synthesis and high-throughput characterization of thin-film materials libraries combined with computational methods. *npj Computational Materials*, 5(1):70, 2019.
25. Martin L Green, CL Choi, JR Hattrick-Simpers, AM Joshi, I Takeuchi, SC Barron, E Campo, T Chiang, S Empedocles, JM Gregoire, et al. Fulfilling the promise of the materials genome initiative with high-throughput experimental methodologies. *Applied Physics Reviews*, 4(1):011105, 2017.
26. Aaron G Kusne, D Keller, A Anderson, A Zaban, and I Takeuchi. High-throughput determination of structural phase diagram and constituent phases using grendel. *Nanotechnology*, 26(44):444002, 2015.
27. Valentin Stanev, Velimir V Vesselinov, A Gilad Kusne, Graham Antoszewski, Ichiro Takeuchi, and Boian S Alexandrov. Unsupervised phase mapping of x-ray diffraction data by nonnegative matrix factorization integrated with custom clustering. *npj Computational Materials*, 4(1):43, 2018.

28. Carla P Gomes, Junwen Bai, Yexiang Xue, Johan Björck, Brendan Rappazzo, Sebastian Ament, Richard Bernstein, Shufeng Kong, Santosh K Suram, R Bruce van Dover, et al. Crystal: a multi-agent ai system for automated mapping of materials' crystal structures. *MRS Communications*, pages 1–9, 2019.
29. W. B. Park, J. Chung, J. Jung, K. Sohn, S. P. Singh, M. Pyo, N. Shin, and K.-S. Sohn. Classification of crystal structure using a convolutional neural network. *IUCrJ*, 4(4):486–494, July 2017.
30. Felipe Oviedo, Zekun Ren, Shijing Sun, Charles Settens, Zhe Liu, Noor Titan Putri Hartono, Savitha Ramasamy, Brian L DeCost, Siyu IP Tian, Giuseppe Romano, et al. Fast and interpretable classification of small x-ray diffraction datasets using data augmentation and deep neural networks. *npj Computational Materials*, 5(1):1–9, 2019.
31. Jin-Woong Lee, Woon Bae Park, Jin Hee Lee, Satendra Pal Singh, and Kee-Sun Sohn. A deep-learning technique for phase identification in multiphase inorganic compounds using synthetic xrd powder patterns. *Nature Communications*, 11(1):1–11, 2020.
32. Jonathan Kenneth Bunn, Shizhong Han, Yan Zhang, Yan Tong, Jianjun Hu, and Jason R. Hattrick-Simpers. Generalized machine learning technique for automatic phase attribution in time variant high-throughput experimental studies. *Journal of Materials Research*, 30(7):879–889, April 2015.
33. David Rossouw, Pierre Burdet, Francisco de la Pena, Caterina Ducati, Benjamin R Knappe, Andrew EH Wheatley, and Paul A Midgley. Multicomponent signal unmixing from nanoheterostructures:overcoming the traditional challenges of nanoscale x-ray analysis via machine learning. *Nano letters*, 15(4):2716–2720, 2015.
34. Ronan Le Bras, Richard Bernstein, John M Gregoire, Santosh K Suram, Carla P Gomes, Bart Selman, and R Bruce Van Dover. Challenges in materials discovery—synthetic generator and real datasets. In *Twenty-Eighth AAAI Conference on Artificial Intelligence*, 2014.
35. Di Chen, Yexiang Xue, Shuo Chen, Daniel Fink, and Carla Gomes. Deep multi-species embedding. In *IJCAI*, 2017.
36. Brian L Sullivan, Jocelyn L Aycrigg, Jessie H Barry, Rick E Bonney, Nicholas Bruns, Caren B Cooper, Theo Damoulas, André A Dhondt, Tom Dietterich, Andrew Farnsworth, et al. The ebird enterprise: an integrated approach to development and application of citizen science. *Biological Conservation*, 169:31–40, 2014.
37. William J Sutherland, Steven Broad, Stuart HM Butchart, Stewart J Clarke, Alexandra M Collins, Lynn V Dicks, Helen Doran, Nafeesa Esmail, Erica Fleishman, Nicola Frost, et al. A horizon scan of emerging issues for global conservation in 2019. *Trends in ecology & evolution*, 2018.

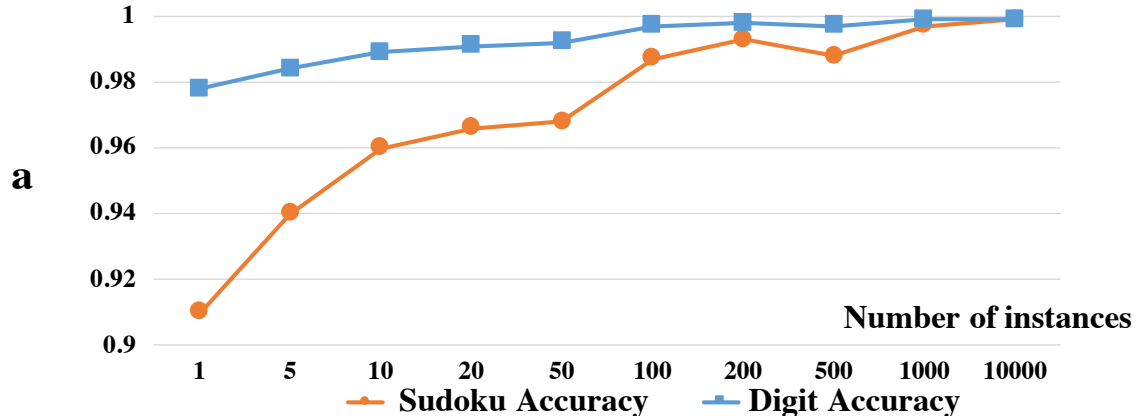
38. Mehdi Mirza and Simon Osindero. Conditional generative adversarial nets. *arXiv preprint arXiv:1411.1784*, 2014.
39. Zhiting Hu, Xuezhe Ma, Zhengzhong Liu, Eduard Hovy, and Eric Xing. Harnessing deep neural networks with logic rules. *arXiv preprint arXiv:1603.06318*, 2016.
40. Jingyi Xu, Zilu Zhang, Tal Friedman, Yitao Liang, and Guy Van den Broeck. A semantic loss function for deep learning with symbolic knowledge. *arXiv preprint arXiv:1711.11157*, 2017.
41. Jiaxuan You, Rex Ying, Xiang Ren, William L Hamilton, and Jure Leskovec. Graphrnn: Generating realistic graphs with deep auto-regressive models. *arXiv preprint arXiv:1802.08773*, 2018.
42. Diederik Kingma and Jimmy Ba. Adam: A method for stochastic optimization. *arXiv preprint arXiv:1412.6980*, 2014.

## **Extended Data**

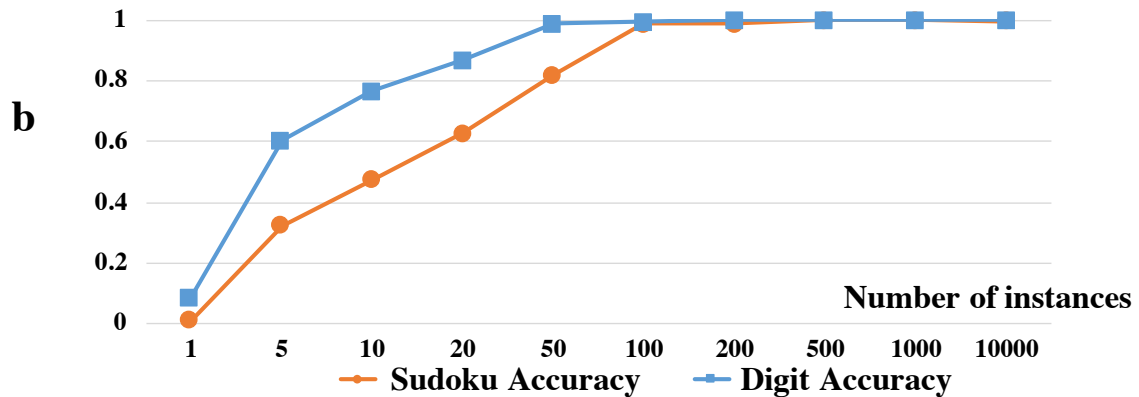


Extended Data Figure 1: **The transformation flow for Deep Reasoning Networks and examples of continuous relaxations.** **a.** The process of formulating a problem into the DRNets framework. (i) We start by formulating tasks as data-driven constrained optimization problems, with discrete and continuous variables. For example, the data-driven constrained optimization task in MNIST-Sudoku is to demix images of two overlapping Sudokus such that the demixed Sudokus satisfy the Sudoku constraints and their reconstruction loss is minimized. Furthermore, in this formulation for MNIST-Sudoku, we assume that a the generative decoder (cGAN) reconstructs the demixed Sudoku digit images using a two-part latent space that encodes the digit probabilities and shapes and that the two-part latent space is produced by two convolutional neural networks (ResNet) and is subject to the Sudoku constraints. (ii) This data-driven constrained optimization problem is converted into a data-driven unconstrained optimization problem using Lagrangean relaxation, which essentially moves the constraints to the objective function, with associated penalty weights. (iii) We use entropy-based continuous relaxations to encode and replace discrete (non-differentiable) constraints with continuous functions, such as sparsity, cardinality, the all-different constraint, and logical constraints. The objective function combines two components: the reconstruction loss of the generative decoder (which for Sudoku corresponds to the reconstruction of the demixed overlapping digit images), and the reasoning loss (which for Sudoku corresponds to the penalty weighted entropy-based continuous function that capture the Sudoku rules). The result of these transformations is the DRNets data-driven unconstrained optimization formulation. (iv) DRNets optimize the overall objective function using constraint-aware stochastic gradient descent (SGD). Note that we refer to these problems as *data-driven* problems since although we assign semantics to the structured latent-space (probabilities and shapes), their full meaning is ultimately determined by the data. **b.** Examples of the continuous relaxation of discrete constraints.  $e_{i,j}$ ,  $P_i$ ,  $Q_i$ ,  $P_M$ , and  $H$ , represent indicator variables denoting if a given input image contains a given digit, the discrete distribution over digits 1 to 4, the discrete distribution over digits 5 to 8, the discrete distribution over values 1 to  $M$ , and the entropy function, respectively. See notation and further details in [Supplementary Methods](#).

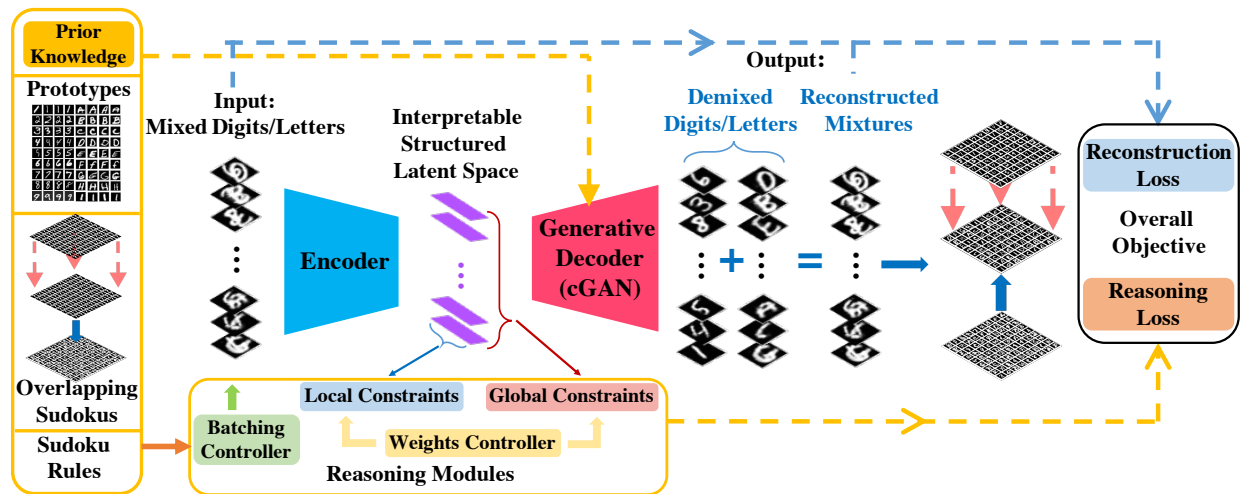
### Performance of DRNets on 4x4 Multi-MNIST-Sudoku with Different Dataset Scales



### Performance of DRNets on 9x9 Multi-MNIST-Sudoku with Different Dataset Scales



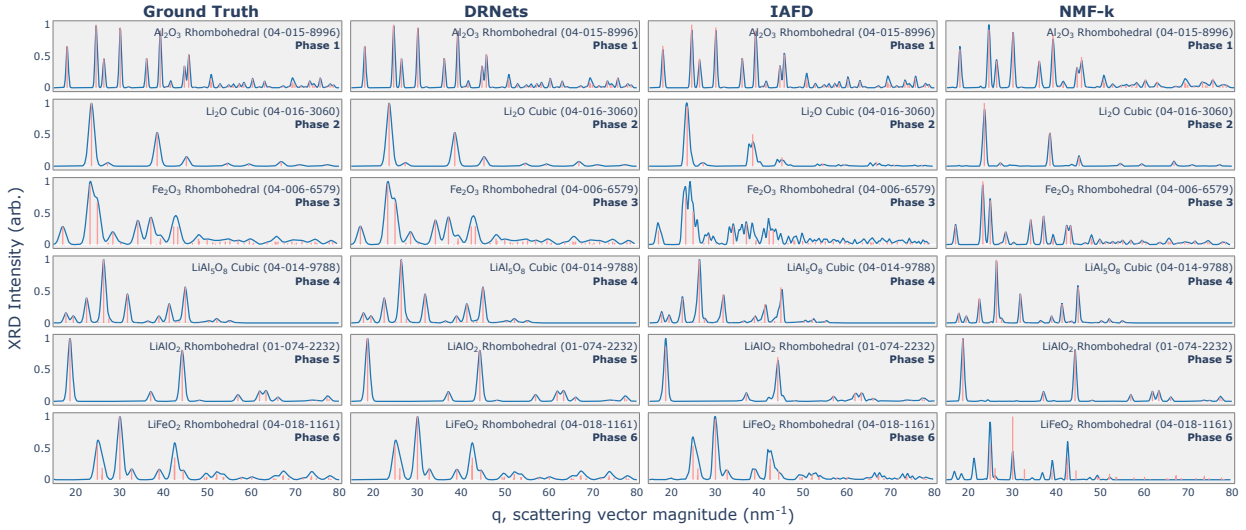
Extended Data Figure 2: **The performance of DRNets on Multi-MNIST-Sudoku tasks with different dataset scales.** Learning over multiple instances significantly (especially, for the 9x9 cases) improves the performance of DRNets. Nevertheless, DRNets can reach 99% Sudoku accuracy with only 100 Multi-MNIST-Sudoku instances, a considerable smaller amount of data compared to standard deep learning approaches.



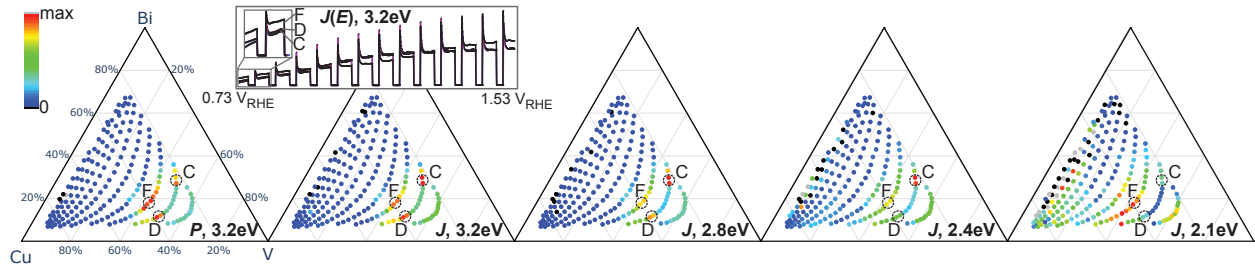
**Extended Data Figure 3: DRNets for Multi-MNIST-Sudoku** DRNets perform end-to-end deep reasoning by using a convolutional neural network to encode an *interpretable* structured latent space that is used by a fixed generative decoder, a conditional generative adversarial network (cGAN), to reconstruct the input mixed digits. The interpretable structured latent space also allows the encoding of reasoning constraints, which enforce that the latent space adheres to prior knowledge about Sudoku rules. Prior knowledge also includes digit prototypes, which are used to pre-train and build the fixed decoder's generative module. An overall objective combines responses from the fixed generative decoder and the reasoning module and is optimized using constraint-aware stochastic gradient descent and backpropagation.

	Methods	Accuracy (%)		Time	Training Set Size	Test Set Size
		Digit	Sudoku			
4x4 Multi-MNIST Sudoku	DRNets	99.90	98.55	28min	N/A	16x10,000 overlapping digits
	DRNets w/o Reasoning <b>(ablation)</b>	88.83	15.01	110min		
	DRNets w/o cGAN <b>(ablation)</b>	16.02	0.0	57min		
	DRNets + exhaustive search	<b>100.0</b>	<b>100.0</b>	5.3hours + 28min		
9x9 Multi-MNIST Sudoku	CapsuleNet	97.87	50.92	1min + 30min	16x10,000 overlapping digits	81x10,000 overlapping digits
	CapsuleNet + local search1	97.87	57.80	3hours + 30min		
	CapsuleNet + exhaustive search	<b>100.0</b>	<b>100.0</b>	5.3hours + 30min		
	ResNet-18	97.67	68.47	3min + 2.6hours		
	ResNet-18 + local search1	97.67	88.31	3hours + 2.6hours		
	ResNet-18 + exhaustive search	<b>100.0</b>	<b>100.0</b>	5.3hours + 2.6hours		
4x4 Multi-MNIST Sudoku	DRNets	<b>99.99</b>	<b>99.23</b>	7hours	N/A	81x10,000 overlapping digits
	DRNets + local search2	<b>99.99</b>	<b>99.84</b>	60s + 7hours		
	DRNets w/o Reasoning <b>(ablation)</b>	63.82	0.0	7hours		
	DRNets w/o cGAN <b>(ablation)</b>	1.24	0.0	7hours		
	CapsuleNet	99.10	23.33	150s + 41hours		
	CapsuleNet + local search2	99.10	73.63	210s + 41hours		

Extended Data Figure 4: **Comparison of the performance of different methods for Multi-MNIST-Sudoku** We show the “solving time” for unsupervised DRNets and its ablation variants and “test time + training time” for supervised baselines. The test time for CapsuleNet/ResNet + local search includes the local search time. Note that we used two different local search algorithms for 4x4 cases and 9x9 cases. "local\_search1" performs an enumeration for the top-2 likely digits in all 16 cells to try to satisfy Sudoku rules. For 9x9 cases, it is impossible to enumerate the top-2 likely digits for 81 cells ( $2^{81}$ ). Therefore, "local\_search2" conducts a depth-first search for digits in each cell from most likely to less likely until it finds a valid Sudoku combination, which is faster than "local\_search1". For 4x4 cases, we also applied exhaustive search for all methods, where we enumerate all possible 4x4 Sudokus and return the one with the highest likelihood given our predictions. Note that such strategy is not feasible for 9x9 Sudokus, given there are around  $6.67 \times 10^{21}$  9x9 Sudokus. The ablation study of removing the reasoning modules (DRNets w/o Reasoning) shows that not only does the Sudoku accuracy degrades, the digit accuracy also degrades, especially for 9x9 Sudokus. The ablation study of replacing the cGAN with a (weaker) standard learnable decoder, without prior knowledge about single digits (DRNets w/o cGAN) shows that both the Sudoku and digit accuracy degrades dramatically.



**Extended Data Figure 5: Comparison of the phase patterns discovered by different methods vs. the ground truth phases for the Al-Li-Fe oxide system.** For each phase we plot the pattern of the reconsolidated phase and the ICDD stick patterns. While the phases discovered by DRNets closely match the ground truth phases, some of the IAFD and NMF-k's phases do not match well the ground truth phases (e.g., phase 3 (IAFD) and phase 6 (NMF-k)); also reflected in the phase fidelity loss (0.00002 (DRNets); 11.920 (IAFD); and 46.156 (NMF-k)); see also Fig. 6a).



**Extended Data Figure 6: Characterization of Bi-Cu-V oxide library for photoelectrocatalysis of the oxygen evolution reaction, a critical reaction for solar fuels technology.** After XRD and XRF measurements, a grid of compositions was characterized with chronoamperometry (CA) with 4 different light emitting diode (LED) illumination sources from which photocurrent ( $J$ ) is calculated, as well as cyclic voltammetry with 3.2 eV illumination (CV) from the photoelectrochemical power generation ( $P$ ) is calculated. The resulting 5 performance metrics are plotted with respect to composition, and select pairs of points from 3 different phase fields in Extended Data Figure 5 are indicated with labels C, D and F. The common false color scale from 0 to a maximum value is used for each metric, with maximum values of  $1.8 \text{ mW cm}^{-2}$  for  $P$  and  $13.3, 14.1, 0.5, 0.045 \text{ mA cm}^{-2}$  for  $J$  with 3.2, 2.8, 2.4 and 2.1 eV illumination, respectively. The anodic sweep of the CV is shown for 3 select samples labeled by their phase region. All 3 of these regions contain  $\text{BiVO}_4$ , a well-known metal oxide photoanode, with much higher Cu concentration than typical Cu-free  $\text{BiVO}_4$  photoelectrocatalysts. All 3 noted phase regions contain  $\text{BiVO}_4$  and  $\text{Cu}_3(\text{VO}_4)_2$  with D and F additionally containing  $\text{Cu}_2\text{BiVO}_6$  and  $\text{Cu}_2\text{V}_2\text{O}_7$ , respectively. The different compositions and phase combinations lead to different performances, in particular the 3 phase region F exhibits higher photocurrent at low applied bias (see inset) and higher photocurrent with 2.1 eV illumination, which are 2 critical properties for  $\text{BiVO}_4$  photoanodes that have been historically difficult to optimize. Despite common belief that phase mixtures are deleterious to photoactivity, these results demonstrate alloying and optimal phase mixtures as promising directions for photoanode discovery and optimization.

Task	Prior Knowledge	Semantics of latent space	Encoder	Generative Model in Decoder	Loss Function
Multi-MNIST-Sudoku ( $n \times n$ overlapping Sudokus)	Overlapping Sudokus Sudoku Rules Single digit training data	1 – Probability of possible digits for each of the two overlapping digits 2 – Shape embeddings of possible digits for each of the two overlapping digits	1 – ResNet-18 with $2 \times n$ output units 2 – ResNet-18 with $2 \times n \times 100$ output units	Conditional GAN (trained on single digits)	Reconstruction loss: L1 norm Reasoning: entropy-based constraints enforcing Sudoku rules
Crystal-Structure Phase Mapping ( $m$ known phases)	Thermodynamic rules Prototype stick patterns (ideal experimental phases) for known crystal phases Phases captured by GMM	1 – Probability of known phases 2 – Variance/Shifting embeddings of known ICDD stick patterns, i.e., estimate of parameters ( $\sigma$ , shift, intensity variance) for GMM	1 - 3-layer-MLP with $m$ output units 2 - Three 3-layer-MLPs with $m, m, m \times K$ output units ( $K$ denotes the maximum number of sticks)	Gaussian Mixture Model + Prototype Stick Patterns	Reconstruction loss: JS-distance + L2 loss Reasoning Loss: entropy-based constraints for thermodynamic rules.

Extended Data Figure 7: **Different components of DRNets for the different tasks.**

## Supplementary Note

**Performance of DRNets for Multi-MNIST-Sudoku:** DRNets significantly outperform CapsuleNet and ResNet, even when these supervised systems are coupled with local search to incorporate Sudoku rules. This is particularly true when going from 4-by-4 to 9-by-9 Multi-MNIST-Sudoku instances: DRNets' digit and Sudoku accuracy for 9-by-9 instances is close to 100%, while ResNet's Sudoku accuracy is around 35%. More comprehensive comparisons are provided in Extended Data Fig. 4.

**Ablation studies for Multi-MNIST-Sudoku:** We performed ablation studies of DRNets on the Multi-MNIST-Sudoku task to demonstrate the importance of the reasoning module and the generative decoder. As shown in the Extended Data Fig. 4, if we remove the reasoning modules, both the Sudoku accuracy and the digit accuracy would drop significantly, which shows that not only does the reasoning module help the Sudoku accuracy, it also improves the digit accuracy by eliminating impossible digits based on Sudoku rules. This effect is especially significant when it comes to the 9x9 case. In the 9x9 case, we used hand-written letters A-I for the second Sudoku in each overlapping Sudokus, which considerably increase the difficulty of recognizing the digit and the letter purely based on the reconstruction loss. Therefore, once we removed the reasoning module, the Sudoku accuracy dropped from 99.2% to 0% and the digit accuracy also dropped from 99.9% to 63.8%. On the other hand, if we replace the generative decoder (cGAN) with a (weaker) standard learnable decoder, without prior knowledge about single digits, we can no longer connect the semantics of our latent space to the output of the decoder. Therefore, the optimization process can no longer find the right semantics for the latent space, even though the discovered nonsensical digits still follow the Sudoku rules (1.24% digit accuracy, 0% Sudoku accuracy).

To demonstrate the importance of the data-driven learning by optimizing the model over multiple instances using shared parameters, we performed ablation studies of the "down-scalability" of DRNets, i.e., when optimized using only a few data instances (Extended Data Fig. 2). We evaluated the performance of DRNets with different dataset scales ranging from only one instance to 10,000 instances. The study shows the importance of learning the shared parameters across instances. Nevertheless, DRNets can reach 99% accuracy with only 100 (unlabeled) 9x9 Multi-MNIST-Sudoku instances, a considerable smaller amount of data compared to standard deep learning approaches. Since optimizing DRNets on a few instances may result in getting stuck at some local minimals such that the constraints are not all satisfied, we applied a restart mechanism<sup>43</sup> on Multi-MNIST-Sudoku to circumvent this issue. Specifically, since DRNets directly incorporate logical constraints, we can check whether those constraints are satisfied or not at the end of a run. If not, for instances with violated constraints, we re-run the algorithm again on them. In this ablation study, we applied at most 3 "restart" runs for each datasets to get the reported results on Extended Data Fig. 2. Due to the restart mechanism, the performance of DRNets on 10,000 instances are slightly better than the one without restart (Extended Data Fig. 4). Moreover, for the datasets with small scales (<1000), we performed multiple runs with randomly sampled instances to obtain an averaged performance.

## Supplementary Methods

**Multi-MNIST-Sudoku Data description:** For Multi-MNIST-Sudoku, we generated  $n^2 \times 10,000$  ( $n$  is 4 or 9) input data points for each training set, validation set and test set, where each data point corresponds to a 32x32 image of overlapping digits/letters from MNIST<sup>20</sup> and EMNIST<sup>21</sup> and every batch of  $n^2$  data points forms a n-by-n overlapping Sudokus. For the 9x9 case, to distinguish the two overlapping Sudokus, we used letters A-I from EMNIST for the second Sudoku. For ease of presentation, we may still refer to letters as "digits" in the following content. We generated an extra *cGAN* dataset, which is composed of 25,000 *original MNIST/EMNIST images* for training the conditional GAN. Note that these four datasets are generated using disjoint sets of digit images.

**DRNets for Multi-MNIST-Sudoku:** For Multi-MNIST-Sudoku, the encoder is made of two ResNet-18 models<sup>23</sup> adapted from the PyTorch source code. The output layer for the first network has  $2n$  ( $n$  is 4 or 9) dimensions, which models the two distributions  $P_i$  and  $Q_i$  for the two overlapping digits. Another network outputs  $2n$  100-dimensional (200n dimensions in total) latent encoding  $\mathbf{z}_{i,j}$  to encode the shape of the possible  $2n$  digits conditioned on the input mixture, and is used by the generative decoder to generate the reconstructed digits. We use a conditional GAN<sup>38</sup>, as the generative model in our generative decoder (for ease of presentation, we abuse a bit the notation of  $G(\cdot)$  to also denote the generative model), which is adopted from the implementation of<sup>44</sup> and pre-trained using digits in the *cGAN* dataset. Note that this is the only supervision we have in this task, which is even weaker than the general concept of the *weakly-supervised setting*<sup>45</sup>. Given the *shape* ( $\mathbf{z}_{i,j}$ ) and *probability* embeddings ( $P_i$  and  $Q_i$ ), DRNets estimate the two digits in the cell by computing the expected digits over  $P_i$  and  $Q_i$ , i.e.,  $\sum_{j=1}^n P_{i,j}G(\mathbf{z}_{i,j})$  and  $\sum_{j=1}^n Q_{i,j}G(\mathbf{z}_{i,j+4})$ , and remix them to reconstruct the original input mixture (Fig. 1g-i and Fig. 2a). We use entropy-based functions to impose the continuous relaxation of the cardinality and All-Different constraints to reason about the Sudoku structure, which results in a total of  $2n^2 + 6n$  constraints for the nxn Sudoku ( $n^2 \times 2$  cardinality constraints enforcing a single digit per cell;  $n \times 3 \times 2$  all-different constraints enforcing no repetition of a digit in a row, column, and box (see Extended Data Fig. 1b).

**Continuous Relaxations for Multi-MNIST-Sudoku:** In Multi-MNIST-Sudoku, there are two types of constraints in the Sudoku rules: (1) *cardinality constraints* and (2) *All-different constraints*.

**Cardinality Constraints:** One straightforward encoding of the discrete version of cardinality constraints, which are used to encode the possible two digits in the cell indicated by data point  $x_i$  (one from  $\{1\dots4\}$  and the other from  $\{5\dots8\}$ ), is to use 8 binary variables  $e_{i,j} \in \{0, 1\}$ , while requiring  $\sum_{j=1}^4 e_{i,j} = 1$  and  $\sum_{j=5}^8 e_{i,j} = 1$ . To relax the discrete variables, DRNets model probability distributions  $P_i$  and  $Q_i$  over digits 1 to 4 and 5 to 8 respectively:  $P_{i,j}, j=1\dots4$  and  $Q_{i,j}, j=1\dots4$  denote the probability of digit  $j$  and the probability of digit  $j + 4$ , respectively. Then, we can approximate the cardinality constraint of  $e_{i,j}$  by minimizing the entropy of  $P_i$  and  $Q_i$ , which encourages  $P_i$  and  $Q_i$  to collapse to one value. One can see, when the entropy of distributions  $P_i$  and  $Q_i$  reaches 0, all the probability mass collapses to only one variable. Therefore, all  $P_{i,j}$  and  $Q_{i,j}$  are either 0 or 1,

which is a valid solution of the original discrete constraints.

**All-different Constraints:** Another combinatorial constraint in Multi-MNIST-Sudoku is the All-Different constraint, where all the cells in a *constrained set*  $S$ , i.e., each row, column, and any of four 2x2 boxes involving the corner cells, must be filled with non-repeating digits. For a probabilistic relaxation of the All-Different constraint, we analogously define the entropy of the averaged digit distribution for all cells in a constrained set  $S$ , i.e.,  $H(\bar{P}_S)$  :

$$H(\bar{P}_S) = - \sum_{j=1}^4 \bar{P}_{S,j} \log \bar{P}_{S,j} = - \sum_{j=1}^4 \left( \frac{1}{|S|} \sum_{i \in S} P_{i,j} \right) \log \left( \frac{1}{|S|} \sum_{i \in S} P_{i,j} \right) \quad (3)$$

In this equation, a larger value implies that the digits in the cells of  $S$  distribute more uniformly. Thus, we can analogously approximate All-Different constraints by maximizing  $H(\bar{P}_S)$  and  $H(\bar{Q}_S)$  while minimizing all  $H(P_i)$  and  $H(Q_i)$ ,  $i \in S$  (for the cardinality constraints of cell- $i$ ). When the entropy of the digit distribution in each cell is 0, we know that the digit distribution of each cell converges to one digit. Hence, if  $H(\bar{P}_S)$  reaches its maximum, i.e.,  $\log |S|$ , we have  $\frac{1}{|S|} \sum_{i \in S} P_{i,j} = \frac{1}{|S|}$  for all digit  $j$ . Crossed with the fact that  $P_{i,j}$  are either 0 or 1 when the cardinality constraints are satisfied, we know that only one  $P_{i,j}$  is equal to 1 for all cell  $i$  in the set  $S$  and others are 0, which directly states the All-Different constraints.

**Baselines for Multi-MNIST-Sudoku:** We compared DRNets with the state-of-the-art for demixing digits, which are supervised methods: CapsuleNet<sup>22</sup> and ResNet<sup>23</sup>. Though ResNet and CapsuleNet have access to labeled data, they do not utilize Sudoku rules. Therefore, to saturate their performance, we further imposed Sudoku rules into those baselines via a post-process. Specifically, for 4x4 cases, we did a local search for the top-2 (top-3 would take too long to search) most likely choice of digits for each Sudoku of the two overlapping Sudokus and try to satisfy Sudoku rules with minimal modification compared with the original prediction. Since there are only 288 different 4x4 Sudokus, we also performed an exhaustive search, which explicitly considers all the possible Sudoku configurations and selects the most likely one. However, such a strategy is out of the question for 9-by-9 instances, given that there are around  $6.67 \times 10^{21}$  possible 9x9 Sudokus. For 9x9 cases, we conduct a different local search algorithm since enumerating the top-2 digits for an 9x9 Sudoku is not feasible ( $2^{81}$ ). We conducted a depth-first search for digits in each cell from most likely to less likely until it finds a valid Sudoku.

Because CapsuleNet<sup>22</sup> did not provide a source code, we adopted the implementation of Laodar<sup>46</sup>, with minor modifications. For ResNet, we adopted the ResNet-18 architecture<sup>23</sup> and trained it in a multi-class classification setting, where we provide explicit supervision for the labels of two digits (one from {1..4} and the other from {5..8}) in each cell. We did a grid search for the hyper-parameters of both baseline models to saturate their performance. Extended Data Fig. 4 shows the comparison of the performance of different methods for Multi-MNIST-Sudoku showing how DRNets outperforms other approaches and how it even has the capability of self-learning by reasoning about the Sudoku rules.

For the training of DRNets, we used  $L1$  loss as the reconstruction loss between the reconstructed mixture and the original input. For the initial weights of constraints, we set 0.01 for the cardinality constraints, 1.0 for the All-Different constraints, and 0.001 for the  $L1$  loss. Note that, DRNets are really "self-supervised"<sup>47</sup> by the Sudoku rules and the self-reconstruction, instead of the standard supervision by labeled data. Therefore, we can directly use DRNets to solve the test set without using a training set. We optimize DRNets on the test set for 100 epochs with a batch size of 100, and it took 50 minutes to finish and achieve the reported performance for the 10,000 overlapping Sudokus.

**Crystal-Structure Phase-Mapping** We illustrate the DRNets for crystal structure phase mapping for two chemical systems: (1) a ternary **Al-Li-Fe** oxide system, described in Le Bras et. al.<sup>34</sup>, which is synthetically generated from a known phase diagram, which also provides the ground-truth solution, and (2) an experimental system from a continuous composition spread thin film from the ternary **Bi-Cu-V** oxide system.

For each system, the input data points are XRD patterns, each containing signals from 1 to 3 phases, as well as the composition of each system. Each XRD pattern is the (nonnegative) XRD scattering intensity as a function of the scattering vector magnitude,  $Q$ . A peak in the XRD pattern results from Bragg scattering and indicates the presence of a plane of atoms in the crystal structure with interplanar spacing of  $d = 2\pi/Q$ . Alloying refers to chemical substitution within a crystal structure where a change in composition causes the crystal structure to stretch or contract, so an expansion by 1% would cause the  $d$  values of the peaks to "shift" multiplicatively by 1%, corresponding to 1% decrease in the  $Q$  value of each peak. Alloying can occur with negligible expansion/contraction of the crystal structure, in which case it cannot be directly detected by measured peak positions. Complex alloying may occur where alterations to the aspect ratio of the crystal structure causes nonuniform peak shifting, which can be modelled by DRNets but was not in the present work. A phase diagram comprises a graph of the regions of composition space where each combination of phases is observed (the phase fields), as well as annotation of any alloying that occurs within each region.<sup>48</sup> DRNets provide all phase fields within the hull of input XRD pattern compositions, as well as peak shifting for each phase that captures most instances of alloying.

Ternary compositions are plotted in a standard 2-D Euclidean triangle plot and Delaunay triangulation provides edges representing neighboring composition points, which is used to establish the mathematical expression of the thermodynamic rules. The mathematical descriptions of our implementations of these rules are described below. The rules result from considering free energy thermodynamics in the context of a composition space with pressure and temperature held constant, as they were in the synthesis of the materials. The names and brief description of the rules are as follows: "Gibbs" is based on the standards Gibbs' Phase Rule and limits the number of phases that can coexist; "Gibbs-Alloy" is an extension of the same thermodynamic rule where the thermodynamic degree of freedom assumed by alloying lowers the max phase count; "Phase-Field-Connectivity" is the composition graph implementation of the definition of a phase field in a phase diagram, i.e. that each phase field comprises a continuous region of composition space. These

thermodynamic rules are central to phase diagram determination<sup>48;49</sup> and have been implemented in different ways in our previous work,<sup>28</sup> and incorporated to some extent in Refs<sup>27</sup> and<sup>26</sup> (e.g. with sparsity constraints and clustering that lowers the number of activated phases).

For the Bi-Cu-V oxide system, the thin film materials were prepared by sputter co-deposition from Bi, Cu, and V sources. The positions of the sources form an equilateral triangle with a substrate above the center on the triangle collecting atoms at different rates at each position, as described previously<sup>50</sup>. At each substrate location the unique mixture or composition of Bi, Cu and V atoms are mixed at the atomic level and crystallize into crystal domains generally between 5 and 100 nm upon subsequent annealing (550 °C in air in this case), forming a thin film approximately 200 nm in thickness. For a given 1 mm<sup>2</sup> area representing a given composition, the mixture of order 10<sup>10</sup> crystal domains comprising the 1 to 3 different phases are characterized through synchrotron x-ray diffraction<sup>51</sup> to generate the XRD pattern for that composition.

There are 307 composition data points for Bi-Cu-V system and each XRD pattern contains  $D = 300$  diffraction signals equally spaced from  $Q=5$  to  $45 \text{ nm}^{-1}$ . There are 231 composition data points for the benchmark Al-Li-Fe system and each XRD pattern contains  $D = 650$  diffraction signals equally spaced from  $Q=15$  to  $80 \text{ nm}^{-1}$ . Each XRD pattern is normalized to a maximum intensity of 1. The set of prototype stick patterns for each system correspond to known crystal structures from the International Centre for Diffraction Data (ICDD) database.

**DRNets for Phase-Mapping:** Given the input  $D$ -dimensional XRD pattern, we use four 3-layer-fully-connected networks as our encoder to encode a two-part latent space, which captures the probabilities (denoted as  $P_{i,j}$ ) and shapes of the possible phases (denoted as  $\mathbf{z}_{i,j}$ ) and is constrained by the reasoning module to satisfy the thermodynamic rules (Fig. 2). To model more realistic conditions, the generative decoder of the DRNets uses Gaussian mixture models<sup>52</sup> to approximate the measured phase patterns where the relative peak locations and intensities are given by the prototype stick pattern, and the latent encoding  $\mathbf{z}_{i,j}$  parameterizes the other information needed to simulate an XRD pattern with a series of Gaussian peaks: the peak width, multiplicative shift of peak locations, and possible amplitude variance. The set of phase activations sum to 1 and are the relative intensities of the set of generated phase-pure patterns whose sum is the reconstruction of the input XRD pattern. To remove negligible activations that are mainly caused by experimental noise we applied a simple post-processing that cuts-off all the activations that are lower than 1.0%. The output of the first three networks in the encoder are  $M$ -dimensional vectors:  $(P_{i,1}, \dots, P_{i,M})$ ,  $(\alpha_{i,1}, \dots, \alpha_{i,M})$ ,  $(\sigma_{i,1}, \dots, \sigma_{i,M})$  ( $M$  is the number of possible phases, e.g., 159 for the Al-Li-Fe oxide system), which represent the probability  $P_{i,j}$  of each phase- $j$  at data point  $i$ , the multiplicative shifting ratio  $\alpha_{i,j}$ , and the standard deviation  $\sigma_{i,j}$  of the Gaussians characterizing the peaks in phase- $j$ , respectively. The output of the last network is a  $M \times K$ -dimensional vector, representing the possible amplitude variance of peaks in each phase. Here,  $K$  is the number of maximal peaks in a stick pattern ( $K = 200$ ). For the first 3 networks there are 1024, 1024, and 512 hidden units, respectively per layer, and for the last network there are 512, 512, and 32 hidden units, respectively per layer. The last layer has fewer hidden units given its high-dimensional output space ( $M \times K$ ).

All networks use ReLU<sup>53</sup> as their activation function.

The thermodynamic rules can concern many to all points in the composition graph, creating a challenging set of combinatorial constraints to impose. In Multi-MNIST-Sudoku, where each overlapping Sudoku naturally forms the maximal connected components in the *constraint graph*, we can easily batch every  $n^2$  data points together to reason about the All-Different constraints among them. However, in Crystal-Structure-Phase-Mapping, since the maximal connected component involves all data points in the composition graph, neither batching all data points into the memory nor reasoning about the whole graph is tractable. Therefore, to enforce the connectivity constraint we devised a strategy of sampling the large connected component through many local structures (still connected components) and solve each of them iteratively. Specifically, for each oxide system, we sampled 100,000 paths in the composition graph via Breadth First Search to construct a path pool. Then, for every iteration, DRNets randomly sample a path from the pool and batch the data points along that path (see Fig. 3b). Finally, we only reason about the thermodynamic rules along the path. By iteratively solving sampled local structures (paths) of the "large" maximal component, we can cost-efficiently approximate all global constraints.

**Continuous Relaxations for Crystal-Structure Phase Mapping:** The thermodynamic rules imposed in DRNets are based on standard properties of isothermal compositional diagrams<sup>48:49</sup>. The only constraint applied to each XRD pattern independently is the maximum of 3 phases. This is a consequence of Gibbs' phase rule where the 2 composition degrees of freedom are the thermodynamic variables corresponding to a maximum phase count of 3 at any point within the ternary composition space. An extension of this rule is that alloying removes at least 1 thermodynamic degree of freedom and thus lowers the maximum phase count to 2. Alloying is detected through comparison of the multiplicative shifting parameters (in the DRNets latent space), between neighboring compositions, where a shifted pattern between 2 neighbors that share the same set of phases invokes the Gibbs-Alloy rule where both patterns may contain only 2 phases. The final rule relates to the compositional connectivity of each phase fields, i.e. Phase-Field-Connectivity. Thermodynamic compositional phase diagrams comprise the convex hull of the Gibbs free energy for all phases as a function of composition. The generally parabolic shape of the free energy for each phase implies that if a phase or set of phases appears on the convex hull at one composition, every other composition where it appears can be accessed by a contiguous composition path. Further the amount of the phase, i.e. its activation in the XRD patterns, will vary smoothly in composition space. Importantly, the thin film synthesis of the Bi-Cu-V system can result in non-equilibrium phase behavior. In our experience, from inspection of thousands of XRD patterns of thin films, any deviation from equilibrium typically does not alter the rules as enforced, likely because the alterations correspond to a kinetically impeded phase that is removed from "consideration" in the free energy diagram, or alteration of the effective free energy for a phase, both of which can change which phases are experimentally observed but not the enforced rules. Indeed this is a key reason why phase mapping of experimental systems is required, as opposed to relying on computed free energy diagrams.

**Implementation of thermodynamic rules for Crystal-Structure Phase Mapping:** *Gibbs*: This rule states the maximum number of co-existing phases, which is imposed via the relaxation of the k-sparsity constraints. For the discrete version, we can model the existence of  $M$  possible phases of  $i$ -th data point using binary variables  $e_{i,j}$  ( $j = 1 \dots M$ ), while requiring  $\sum_{j=1}^M e_{i,j} \leq k$ . We derive the relaxation of k-sparsity constraints in a similar way as the cardinality constraints except that we now want to force the distribution to concentrate on at most  $k$  entities (phases). By normalizing the values of discrete variables  $e_{i,j}$  ( $j = 1 \dots M$ ) to a discrete distribution  $P_M$ , we can minimize the entropy of distribution  $P_M$  to at most  $\log k$ , which is the maximal entropy when the distribution concentrates on only  $k$  values. Though,  $H(P_M) < \log k$  is not a sufficient condition for k-sparsity, we can initialize the threshold  $c$  of k-sparsity constraints to  $\log k$  and dynamically adjust the value of  $c$  based on the satisfaction of the k-sparsity constraints. In practice, it works well with the supervision from other modules, such as the self-reconstruction.

**Gibbs-Alloy**: DRNets explicitly model the shifting ratio in the generative decoder and penalize the difference between adjacent data points along our sampled path. The reasoning module keeps track of the difference of shifting ratio between adjacent data points, and when it is larger than a threshold (0.001), we confirm the existence of "alloying" and reduce the maximum number of possible co-existing phases by one via adjusting the threshold  $c$  in the k-Sparsity Constraints.

**Phase-Field-Connectivity**: We impose this rule by penalizing the difference between the phase activation of adjacent data points  $P_u$  and  $P_v$  along the sampled path. In our implementation, we used L2-norm to penalize the difference.

**Evaluation Criteria for Phase Mapping**: Our evaluation criteria (see Fig. 6a) include reconstruction losses, phase fidelity loss and the satisfaction of thermodynamic rules. Note that, before evaluating the reconstruction losses, we fit the demixed patterns (for all methods) to the closest prototype using a model described previously<sup>34</sup> to exclude noise. We quantified the phase fidelity loss by measuring the Jensen-Shannon distance (JS distance) between the demixed XRD pattern and the closest pattern simulated from a prototype. The motivation for using the JS distance metric for fidelity of demixed patterns is that the set of peaks and their locations are the most important characteristics of a phase pattern. We normalize the area under each XRD pattern to be 1 and use the JS distance metric (with  $\epsilon$  of 1e-9 to avoid division by zero) to quantify the difference between two patterns, which has a large loss when peaks appear in one pattern but not the other.

**Manual Solution Evaluation for Phase Mapping**: The detailed explanation of the main text statement “the presence of each phase was manually verified by matching each prototype peak to a signal in a corresponding XRD pattern and by confirming that measured XRD peaks in the pattern are explained by the DRNets solution” is as follows: for powder XRD patterns, all peaks (with intensity above the detectability limit) in the prototype must be in the measured pattern, and all peaks in the XRD pattern must be explained by prototypes. Failure of the former indicates that one is considering a prototype of the wrong crystal structure, and failure of the latter could be due to

the wrong prototype or an undetected phase, so this analysis can only be done once all phases are identified. This is precisely why complex phase mapping in high dimensional composition spaces is intractable for humans because the pure-phase XRD patterns are not known and the existence of peaks from multiple phases creates many different possible choice of prototype(s) that explain some to all of the measured peaks, especially under consideration of possible peak shifting of the prototypes. In many cases, a single XRD pattern can only be definitively solved by reasoning about XRD patterns of related compositions, so finding a logically consistent solution is very difficult.

Phase mapping problems are particularly challenging when the XRD data does not contain examples of pure phase patterns, as is often the case in combinatorial materials research. In the Bi-Cu-V DRNets solution, only 2 of the 13 phases appear with activations above 80%, demonstrating the ability of DRNets to identify prototypes that only appear in combination with other prototypes.

In phase mapping, we also note the possibility of the presence of a phase in the input XRD patterns that is entirely distinct (not just modified) from all prototypes. We don't discuss handling such cases since it is beyond the scope of this work, requiring density function theory analysis, although our results on reconstruction loss (DRNets produces much better data reconstruction than other methods) demonstrate that the presence of a new phase would be readily identifiable by an uncharacteristically high reconstruction loss in a specific composition region.

**Baselines for Crystal-Structure Phase Mapping:** We compared DRNets with the state-of-the-art phase mapping algorithms, IAFD<sup>28</sup> and NMF-k<sup>27</sup>, which are both non-negative matrix factorization (NMF) based unsupervised demixing models. NMF-k improves the pure NMF algorithm<sup>54</sup> by clustering common phase patterns from thousands of runs. However, NMF-k does not enforce thermodynamic rules and therefore the solutions produced are often not completely physically meaningful. IAFD uses external mixed-integer programming modules to enforce thermodynamic rules during the demixing. However, due to the gap between the external optimizer and NMF module, the solution of IAFD is still far from the ground truth.

Our evaluation criteria (see Fig. 6a) include reconstruction losses, phase fidelity loss and the satisfaction of thermodynamic rules. Note that, before evaluating the reconstruction losses, we fit the demixed phases (for all methods) to the closest ideal phases using the physical model<sup>34</sup> to exclude noise. Meanwhile, we quantified the phase fidelity loss by measuring the Jensen-Shannon distance (JS distance) between the demixed phases and the closest ideal phases. The reason of using the JS distance to measure the fidelity is that the location of peaks are the most important characteristics of a phase pattern. We normalize the area under each XRD pattern to be 1 and use the JS distance metric (with  $\epsilon$  of 1e-9 to avoid division by zero) to quantify the difference between two patterns, which has a large loss when peaks appear in one pattern but not the other.

We also considered a recently proposed supervised algorithm<sup>31</sup> in which a deep neural network, trained using simulated data based on known crystal phase patterns, directly predicts the

phases present in a given XRD pattern. While such an approach can be effective for complementing human expertise for a single XRD pattern, it performed poorly on a complex system such as the benchmark Al-Li-Fe oxide system (phase identification accuracy around 1%), which highlights the limitations of a purely simulated-based supervised approach for handling the combinatorics of phase mapping. Moreover, we note that the method can only provide a classification for the existence or the quantized fractions of phases instead of actually estimating the weights (regression task) of the phase activations, as done by DRNets. So, we evaluated DRNets using the setting of their classification tasks on their Li-Sr-Al powder system dataset. We used a similar setting of hyper-parameters as for the Bi-Cu-V oxide system. We note that this powder system only contains one phase combination ( $\text{Li}_2\text{O}$ ,  $\text{SrO}$ , and  $\text{Al}_2\text{O}_3$ ): both their model and DRNets achieved 100% phase recognition accuracy. For the quantized phase fraction (0-33%, 33%-66%, and 66%-100%) classification tasks, unsupervised DRNets have an accuracy of 95.3%, outperforming their supervised model with accuracy of 86.0%. Beyond this quantized phase activation classification, DRNets can further provide estimates of the weights of the phase activations with an average error of 4.7%.

In the optimization process of DRNets, we used the JS distance with a weight of 20.0 plus the L2-distance with a weight of 0.05 as the reconstruction loss. Due to the different noise level in the Al-Li-Fe oxide system and the Bi-Cu-V oxide system, we use different weights for the penalty functions of different constraints. For Al-Li-Fe oxide system, the weights of k-sparsity constraints (Gibbs rule) is 1.0 and the weights of phase field connectivity constraints is 0.01. For Bi-Cu-V oxide system, the weights of k-sparsity constraints (Gibbs rule) is 30.0 and the weights of phase field connectivity constraints is 3.0. In terms of the optimization process, DRNets took about 30 minutes to achieve the reported performance for both systems. In contrast, not only do IAFD and NMF-k have a much worse performance with respect to the solution quality, they also take considerable longer, several hours, to generate their solutions. In fact, for the Bi-Cu-V oxide system, both NMF-k's solution and IAFD's solution are not physically meaningful.

**Down-Scaling Analysis for Crystal-Structure Phase Mapping:** We also investigated the "down-scalability" of DRNets for crystal structure phase mapping tasks, which further confirmed the importance of learning DRNets across multiple samples. In this experiment, we used *phase activation accuracy* as the evalution metric, which evaluates the percentage of sample points that have the same set of phases as the ground truth. For Al-Li-Fe oxide system, we evaluated the performance of DRNets learned over different number of XRD patterns ranging from one XRD patterns to the entire set. For the case of using K XRD patterns, we performed  $\lfloor 231/K \rfloor$  runs of DRNets on the XRD patterns randomly sampled from the composition space to obtain an averaged performance. As shown in Fig. 6, learning over multiple XRD patterns plays an important role for DRNets to solve the Al-Li-Fe oxide system and DRNets can almost perfectly recover the phase activation of XRD patterns when it is learned over more than 150 XRD patterns. Since we do not have the ground truth of the Bi-Cu-V oxide system, we only evaluate the consistency between the results of running DRNets on all 307 XRD samples and the results of running DRNets on each XRD sample one at a time (named DRNet-single). We made minor edition to the DRNet

to adapt to the setting of running on a single XRD pattern. For DRNet-single, we ignored the Gibbs-alloying rule and the phase-field-connectivity rule since they do not make sense on a single sample point. As a result, DRNet-single can only identify the same phases as DRNets for 27% of the patterns, highlighting that the nuanced phase behavior of this system can only be resolved through combinatorial experimentation matched with learning the shared parameters across multiple XRD patterns combined with reasoning about the underlying complex thermodynamic constraints.

## References in Supplementary Methods

43. Carla P Gomes, Bart Selman, Henry Kautz, et al. Boosting combinatorial search through randomization. *AAAI/IAAI*, 98:431–437, 1998.
44. Erik Linder-Noren. Pytorch-gan, 2019.
45. Ning Zhang, Junchi Yan, and Yuchen Zhou. Weakly supervised audio source separation via spectrum energy preserved wasserstein learning. *arXiv preprint arXiv:1711.04121*, 2017.
46. Laodar. A tensorflow implementation for capsnet, 2017.
47. Longlong Jing and Yingli Tian. Self-supervised visual feature learning with deep neural networks: A survey. *arXiv preprint arXiv:1902.06162*, 2019.
48. John F. Smith. Chapter One - Introduction to Phase Diagrams. In J. C. Zhao, editor, *Methods for Phase Diagram Determination*, pages 1–21. Elsevier Science Ltd, Oxford, January 2007.
49. Doreen Edwards. Chapter Ten - Phase Diagram Determination of Ceramic Systems. In J. C. Zhao, editor, *Methods for Phase Diagram Determination*, pages 341–360. Elsevier Science Ltd, Oxford, January 2007.
50. Santosh K Suram, Lan Zhou, Natalie Becerra-Stasiewicz, Kevin Kan, Ryan JR Jones, Brian M Kendrick, and John M Gregoire. Combinatorial thin film composition mapping using three dimensional deposition profiles. *Review of Scientific Instruments*, 86(3):033904, 2015.
51. JM Gregoire, DG Van Campen, CE Miller, RJR Jones, SK Suram, and A Mehta. High-throughput synchrotron x-ray diffraction for combinatorial phase mapping. *Journal of synchrotron radiation*, 21(6):1262–1268, 2014.
52. Bruce G Lindsay. Mixture models: theory, geometry and applications. In *NSF-CBMS regional conference series in probability and statistics*, pages i–163. JSTOR, 1995.
53. Vinod Nair and Geoffrey E Hinton. Rectified linear units improve restricted boltzmann machines. In *Proceedings of the 27th international conference on machine learning (ICML-10)*, pages 807–814, 2010.

54. CJ Long, D Bunker, X Li, VL Karen, and I Takeuchi. Rapid identification of structural phases in combinatorial thin-film libraries using x-ray diffraction and non-negative matrix factorization. *Review of Scientific Instruments*, 80(10):103902, 2009.